

Discovery of disc truncations above the galaxies' mid-plane in Milky Way-like galaxies

Cristina Martínez-Lombilla,^{1,2}★ Ignacio Trujillo^{1,2} and Johan H. Knapen^{1,2,3}

¹*Instituto de Astrofísica de Canarias (IAC), La Laguna, 38205, Spain*

²*Departamento de Astrofísica, Universidad de La Laguna (ULL), E-38200, La Laguna, Spain*

³*Astrophysics Research Institute, Liverpool John Moores University, IC2, Liverpool Science Park, 146 Brownlow Hill, Liverpool, L3 5RF, UK*

Accepted XXX. Received YYY; in original form ZZZ

ABSTRACT

Disc truncations are the closest feature to an edge that galaxies have, but the nature of this phenomenon is not yet understood. In this paper we explore the truncations in two nearby ($D \sim 15$ Mpc) Milky Way-like galaxies: NGC 4565 and NGC 5907. We cover a wide wavelength range from the NUV and optical to $3.6 \mu\text{m}$. We find that the radius of the truncation (26 ± 0.5 kpc) is independent of wavelength. Surprisingly, we identify (at all wavelengths) the truncation at altitudes as high as 3 kpc above the mid-plane, which implies that the thin disc in those outer regions has a width of at least this value. We find the characteristic U shaped radial colour profile associated with a star formation threshold at the location of the truncation. Further supporting such an origin, the stellar mass density at the position of the truncation is $\sim 1\text{--}2 M_{\odot} \text{pc}^{-2}$, in good agreement with the critical gas density for transforming gas into stars. Beyond the truncation, the stellar mass in the mid-plane of the disc drops to just 0.1–0.2% of the total stellar mass of the galaxies. The detection of the truncation at high altitude in combination with the U shape of the radial colour profile allows us to establish, for the first time, an upper limit to the present-day growth rate of galactic discs. We find that, if the discs of these galaxies are growing inside-out, their growth rate is less than $0.6\text{--}1$ kpc Gyr^{-1} .

Key words: galaxies: evolution – galaxies: formation – galaxies: structure – galaxies: stellar content – galaxies: individual: NGC 4565 and NGC 5907 – galaxies: spiral

1 INTRODUCTION

Many discs of spiral galaxies have a well-defined feature in their periphery that is called a truncation. Truncations are found in three out of four galaxy thin discs (van der Kruit & Freeman 2011; Comerón et al. 2012) and typically occur at radial distances of four or five times the exponential scale length of the inner disc. Beyond the truncation the light distribution declines rapidly (van der Kruit 1979; van der Kruit & Searle 1981a,b). The origin of this effective frontier for disc galaxies is yet unclear. Some authors suggest it could be linked to a threshold in star formation (Kennicutt 1989; Roškar et al. 2008b,a), for others, the truncation reflects the location of those stars with the largest angular momentum at the moment of the collapse of the protogalaxy (van der Kruit 1987). Other alternatives in the literature to explain the origin of breaks in the surface brightness distribution of

the discs include bar angular momentum distribution (Debbattista et al. 2006), or any other driver such as density waves, or the heating and stripping of stars by bombardment of dark matter subhaloes (e.g., Laurikainen & Salo 2001; de Jong et al. 2007). In order to probe the nature of this edge, we explore whether its location depends on either the wavelength at which it is measured or the height above the galaxy mid-plane (see e.g., de Jong et al. 2007). The truncation of discs can be seen at any galaxy orientation but, due to its location in the outer disc (and consequently at low surface brightness), an edge-on orientation is the most favoured one (see discussion in Martín-Navarro et al. 2012).

Truncations should not be confused with the surface brightness breaks in Type II surface brightness profiles found at smaller radii (roughly two times closer to the galaxy centre, as reported in the unified picture of breaks and truncations in spiral galaxies proposed by Martín-Navarro et al. 2012). This means that the features labelled as truncations by Pohlen & Trujillo (2006) most probably are disc breaks

★ E-mail: cml@iac.es

rather than the face-on counterparts of truncations observed in edge-on galaxies. In the review by [Debattista et al. \(2017\)](#), breaks are defined as a break in the star formation, not as the bumps and wiggles produced by bars, rings, or spirals inside the disc, while truncations imply a sharp edge. In this work we adopt the assumption of [Martín-Navarro et al. \(2012\)](#), namely that type II breaks correspond to a feature in galaxy discs (mainly connected to a break in star formation) at closer radial distances than the truncations and that, for many (but not all) galaxies, breaks and truncations can coexist as two differentiated features. The ability to detect disc truncations is highly conditioned by the galaxy's orientation. In face-on systems the truncations can be seen only in very deep surface photometry, as they are fainter than in the edge-on view (e.g., [Martín-Navarro et al. 2012](#); [Peters et al. 2017](#)). This is because of the reduced line-of-sight integration through the disc. Nevertheless, truncations can also be hidden by the lopsided nature of spiral galaxies (e.g., [Zaritsky et al. 2013](#)), and/or by light from a faint stellar halo ([Pohlen et al. 2002](#); [Martín-Navarro et al. 2012](#)) and/or from the inner disc scattered by the PSF ([de Jong 2008](#); [Sandin 2014, 2015](#)).

If truncations are connected with an inside-out propagation of star formation in the disc, the expectation is that the location of this feature changes as cosmic time progresses (such cosmic evolution has been observed for the location of type II breaks in disc galaxies since $z \sim 1$, [Trujillo & Pohlen 2005](#); [Azzollini et al. 2008b](#)). If this were the case, the younger populations would be expected to show a truncation at larger radial distances than older populations. Similarly, due to the time delay for the stellar populations originated in the plane of the disc to reach a given distance above the galaxy mid-plane, the location of the truncation at large heights would be expected to occur at smaller radial distances than for stars at the mid-plane. This change in the position of the truncation would depend on its stellar population ages and so its radial position would change gradually. Consequently, one could use the location of the radial truncation of discs to measure ongoing growth (if any) of disc galaxies. We explore these ideas in this paper.

If breaks and truncations had a common origin, predictions in [Roškar et al. \(2008a\)](#) might be relevant. They propose the origin of breaks in an inside-out disc growth scenario, where the stellar disc is formed with a surface density profile consisting of an inner exponential breaking to a steeper outer exponential. The break forms early on and persists in time, moving outward as more gas is able to cool and add mass to the disc. This break is associated to a drop in the cooled gas surface density (i.e., a radial star formation cut-off), while the stellar populations in the outer exponential were scattered outward on nearly circular orbits from the inner disc by spiral arms (i.e., secular evolution processes). A consequence of such a formation and evolution scenario is a sharp change in the radial mean stellar age profile at the break radius, which is in excellent agreement with the observations reported in [Bakos et al. \(2008\)](#). [Roškar et al. \(2008a\)](#) suggest that the location of the break radius evolves with time (see their Fig. 1), while it is independent of the age and of height (see their Fig 3). The simulations thus show that migration forces a common break radius for all stellar populations, even ones born at a time when the break radius was much smaller. We explore this issue here.

Galaxies grow at different speed depending on their mass (see e.g., [Trujillo et al. 2004, 2006](#)). To facilitate the interpretation of the data, we have thus explored two edge-on disc galaxies with masses similar to the Milky Way: NGC 4565 and NGC 5907 ($v_{\text{rot}} \sim 230 \text{ km s}^{-1}$). To probe the ongoing growth of the galaxies it is necessary to have enough spatial and time resolution. The closer the galaxies are, the better the spatial resolution to explore the locations of the truncation as a function of wavelength and/or height. For this reason, we have taken two galaxies that are at a distance less than 20 Mpc. At the typical 1 arcsec resolution from ground-based data, this implies that the minimum difference in spatial location we can resolve is $\sim 100 \text{ pc}$. To probe whether the truncation is moving (i.e., to measure its radial velocity), it is also necessary to have a time estimator. Throughout this work, we will use two different clocks. For the first approach, we use as a proxy to measure time the change in the NUV- r colour of recently formed stellar populations. We will show that intervals of time of just a few hundred Myr can produce variations of such a colour of $\sim 1 \text{ mag}$. The other time indicator we will use is the time that it takes for a star originated in the disc plane to reach a certain height. We will show that at the radial distance of the truncation, the time that a star needs to arrive a few kpc above the disc is (again) a few hundred Myr. These two time indicators, together with our spatial resolution, allow us to measure growth rates with an accuracy better than 0.5 kpc Gyr^{-1} .

Finally, in addition to measuring the growth rate of the disc, finding disc truncations at different heights above the galaxy mid-plane can help to measure the “thickness” of the thin disc. Although the origin of the truncation is not clear, if indeed it is related to a star formation threshold, then the truncation is expected to be a phenomenon linked exclusively with the thin disc. In this sense, if the truncations are clearly visible up to a given height, we could claim with some confidence that at such a radial location the thin disc is still present. Consequently, the highest location at which the disc truncation can be measured can be used as a measure of the vertical extent of the thin disc.

The paper is structured as follows. In Sect. 2 we present our sample, selection criteria, and data. Then, we describe in detail the method and how the profiles are extracted (Sect. 3). The results are shown in Sect. 4 and analysed in Sections 5, 6 and 7. All magnitudes are provided in the AB system.

2 TARGET SELECTION AND DATA

We study the position of the truncation as a function of the height above the mid-plane in the two well-known highly inclined nearby galaxies NGC 4565 and NGC 5907 (see Fig. 1). We cover a wide wavelength range, from the near ultraviolet (NUV) and optical, to the infrared (IR). Table 1 summarizes the general information and physical parameters of both galaxies. For each object, the Hubble type was taken from the *Spitzer* Survey of Stellar Structure in Galaxies (S⁴G, [Sheth et al. 2010](#)) morphological classification of [Buta et al. \(2015\)](#) and the distance was obtained from the most

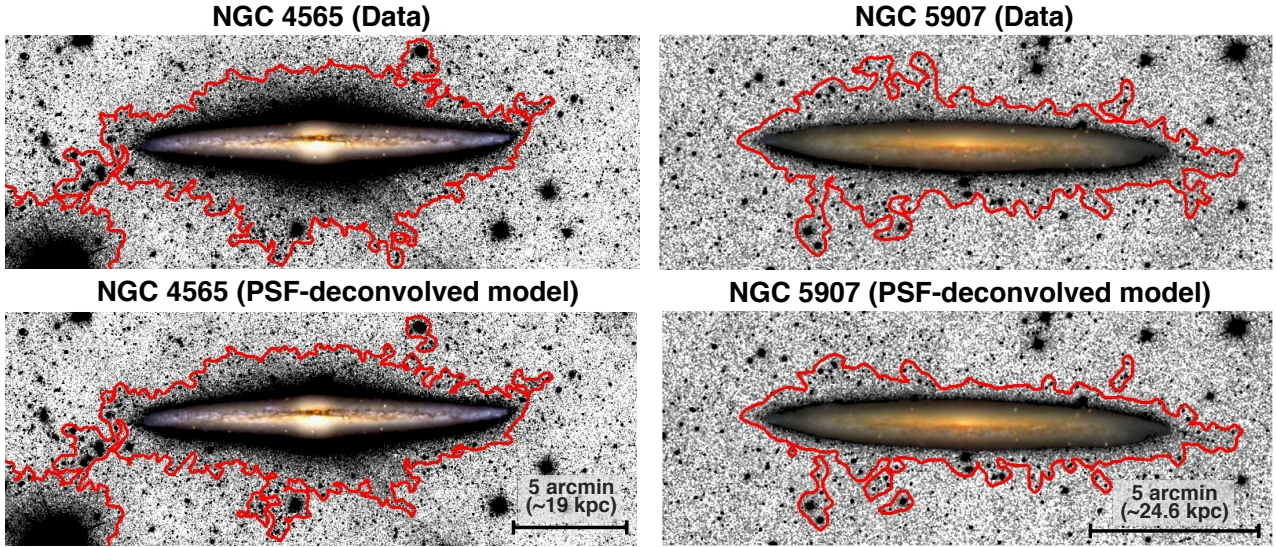


Figure 1. Images of NGC 5907 (left) and NGC 4565 (right) in SDSS *gri* combined light (roughly equivalent to a deep *r*-band image). For illustrative purposes, a colour image obtained with the same telescope has been inserted atop the saturated disc region of the galaxy. Panels show in greyscale and for each galaxy the observed data, in the case of the first row, and the PSF-deconvolved models in the second row (see Sect. 3.4 for details). The colour image of each galaxy is the same for both PSF-convolved and PSF-deconvolved models. Overplotted on all the images are the surface brightness contours (red) corresponding to $27 \text{ mag arcsec}^{-2}$. These contours are located closer to the galaxy's mid-plane when the scattered light is corrected.

recent values in the NASA/IPAC Extragalactic Database¹ (NED). The other properties were taken from the HyperLeda² database (Makarov et al. 2014).

2.1 Selection criteria

The galaxies were selected based on their apparent size, mass, inclination, morphological type and on the availability of images in the wide spectral range considered. In particular, we need galaxies with large apparent sizes ($d_{25} \gtrsim 10 \text{ arcmin}$) in order to reach good physical spatial resolution. We also want very inclined galaxies ($\text{incl} \gtrsim 85 \text{ deg}$) to ensure that our analysis is done in the vertical direction of the object. We choose Milky Way-like galaxies in terms of rotational velocity ($v_{\text{rot}} \sim 230 \text{ km s}^{-1}$, Bland-Hawthorn & Gerhard 2016) but with different morphology (see Table 1). The main reason is that several N-body simulations have shown relations between the sources of internal secular vertical heating and galaxy morphology, such as spiral arms or bars (e.g., Sellwood & Carlberg 1984; Minchev & Quillen 2006; Grand et al. 2016). In this case, the main difference is the presence of a bar in NGC 4565 but not in NGC 5907 (Buta et al. 2015). Finally, we checked Sloan Digital Sky Survey Data Release 12 (SDSS DR12) images (Alam et al. 2015) to avoid galaxies with bright foreground stars or very strong dust lanes.

2.2 GALEX NUV data

The ultraviolet data were taken from the *Galaxy Evolution Explorer* (GALEX, Martin et al. 2005; Morrissey et al. 2007)

Guest Investigator Program (GIP, PI V. Buat; NGC 4565: GI6-049003, NGC 5907: GI6-049002) in the NUV band (1750–2800, 2267 effective wavelength). GALEX images have a circular field of view (FOV) of 1.2 degrees, and a spatial resolution (FWHM) of 5.3 arcsec in the NUV channel sampled with a pixel size of 1.5 arcsec. The exposure times of our images are 12050.15 seconds in fourteen visits for NGC 4565 and 15118.45 seconds in eleven visits for NGC 5907, which gives a surface brightness limit of $\mu_{AB} \sim 30.5 \text{ mag arcsec}^{-2}$ (1σ). To convert intensities to magnitudes, we used the GALEX zero point magnitude from Morrissey et al. (2007), $m_{0,NUV} = 20.96$.

2.3 SDSS optical data

We use optical data from the SDSS DR12 (Alam et al. 2015) in the *g*, *r* and *i* bands. As we are studying extended objects, we used the SDSS mosaic tool³, which stitches together the corrected frames in a selected region to form coherent images over larger patches of the sky. These mosaics were created using the SWARP (Bertin et al. 2002) utility. The resulting images were calibrated and sky-subtracted just as the corrected frames themselves are, but we also estimate our sky background independently (see Sect. 3.2 for more details).

The SDSS survey images have a pixel size of 0.396 arcsec and a mean PSF FWHM value in the *r*-band of 1.3 arcsec. The exposure time for all the images is 53.9 seconds. After combining the *g*, *r* and *i* bands by adding them all together, in order to reach a deeper surface brightness limit, we could to extract reliable surface brightness profiles down to $\mu \sim 27.0 \text{ mag arcsec}^{-2}$ with a fixed zero point value⁴

¹ <http://ned.ipac.caltech.edu/>

² <http://leda.univ-lyon1.fr/>

³ <http://dr12.sdss.org/mosaics/>

⁴ <http://www.sdss.org/dr12/algorithms/magnitudes/>

Table 1. Properties and physical parameters of NGC 4565 and NGC 5907. Columns represent: (1) galaxy ID; (2) morphological type from Buta et al. (2015); (3) distance in Mpc from the average of the most recent values (since 2010) in the NED; (4) major axis position angle (North Eastwards) from the HyperLeda database (Makarov et al. 2014); (5) absolute B -band magnitude (HyperLeda, Makarov et al. 2014); (6) maximum rotational velocity corrected for inclination (HyperLeda, Makarov et al. 2014); (7) galaxy diameter in arcmin at the isophotal level 25 mag arcsec⁻² in the B -band corrected for galactic extinction (HyperLeda, Makarov et al. 2014); and finally, (8) inclination to the line-of-sight in degrees obtained by the authors of this work assuming that the most dense part of the dust lanes of the galaxies are located in the mid-plane.

Galaxy ID	Morph. type	D [Mpc]	PA [deg.]	M_{abs} [B -mag]	v_{rot} [km s ⁻¹]	d_{25} [arcmin]	Incl. [deg]
NGC 4565	SB _X (r)ab spw	13.1 ± 0.5	135.2	-21.44 ± 0.24	243.6 ± 4.7	16.6 ± 0.1	88.5 ± 0.5
NGC 5907	SA:(nd)cd spw	16.9 ± 0.3	155.6	-21.48 ± 0.14	226.6 ± 4.3	11.2 ± 0.1	87.5 ± 0.5

of $m_{0,gri} = 20.49$. We consider a profile reliable if by using $\pm 1\sigma_{sky}$ in the profile extraction, it deviates less than 0.2 mag from the one with the mean sky value (Pohlen & Trujillo 2006). The combined gri profile is roughly equivalent to the r -band profile: we did not find any departure of the gri combined data from the r -band larger than 0.1 mag along the entire radial profile in the region where the photometric uncertainty is negligible.

2.4 Infrared S⁴G data

The S⁴G project (Sheth et al. 2010) obtained 3.6 and 4.5 μm images of 2352 nearby galaxies ($D < 40$ Mpc) using the Infrared Array Camera (IRAC, Fazio et al. 2004). We are particularly interested in the 3.6 μm band (IRAC channel 1) because it is a reasonably good tracer of stellar mass density and the images are less affected by dust. This is a key point when dealing with edge-on galaxies as there is a lot of dust along the line of sight. The S⁴G team have reduced all the data using their pipelines (Muñoz-Mateos et al. 2015; Querejeta et al. 2015; Salo et al. 2015).

The S⁴G IRAC 3.6 μm images have a pixel size of 0.75 arcsec and each galaxy was observed for 240 seconds. The limit in the surface brightness profiles is $\mu \sim 27.0$ mag arcsec⁻² (1σ) using a zero point of $m_{0,S^4G} = 20.472$.

3 METHODOLOGY

3.1 Masking process

Dealing with deep imaging of the outskirts of galaxies requires careful treatment to remove the light from foreground and background objects (see e.g., Trujillo & Fliri 2016). The goal of the masking process is to keep only the flux from the sources we want to analyse, avoiding contamination in their fainter parts. Thus, we mask every fore- and background emission source using a semi-automatic code (see an example in Fig. 2).

First, using SExtractor (Bertin & Arnouts 1996), the code detects the sources in the whole image, and builds a mask with all of them. Then, we use Python-based routines to unmask the galaxy under study. To do that, we convert all the masked areas (except the target) provided from SExtractor to masked pixels. The target is then identified by comparing its coordinates with those of the SExtractor masked regions. Finally, we check visually whether the extent of the mask covers all undesirable flux. For better

inspection, we smooth the images and adjust the contrast to the background limit. This allows us to see if the size of the individual masks is big enough to cover all light from sources that are not our target. If not, we increase each masked area in steps of three pixel dilation to completely avoid all the non-desirable flux. By repeating this process, we are able to remove the background sources from the image. However, some objects that SExtractor has problems to detect can remain visible around the galaxy under study, in its outskirts and even within it (e.g., stars from our Galaxy). To get rid of these, we add masks manually with Python.

This is a common method for all bands, except for the S⁴G data, where the masks were supplied by the S⁴G team (details in Sheth et al. 2010). In this case, we increase the masked areas using the method described above to cover all foreground and background objects when adjusting the contrast to the background limit.

3.2 Sky subtraction and background treatment

We used background-subtracted images from each of the telescopes. However, once the images were masked (see Sect. 3.1), we performed an additional non-aggressive sky subtraction by measuring the background level as in Pohlen & Trujillo (2006). We determined the gradient of a very extended radial surface brightness profile of each galaxy (~ 1.5 times the size of the galaxy), convolved with a one-dimensional Gaussian kernel (1 pixel standard deviation). The mean sky level of each image is the mean value of the most extended part (~ 80 arcsec length) of the radial surface brightness profile in the corresponding flattest region of its gradient function for each galaxy, and this is subtracted from the whole image. As we obtain the sky value from our region of interest through very extended radial surface brightness profiles, this method allows us to identify clearly where a galaxy ends and, consequently, where a profile starts to be dominated by the sky background component. Note that our data were free of large scale gradients in the sky background emission, so the procedures of Peters et al. (2017) are not considered here.

3.3 Profile extraction and truncation position

The galaxy surface brightness profiles in the radial direction were extracted by calculating the flux values along a slit of constant width. The width of the slit was determined in terms of the physical distance (kpc) in the galaxy, de-

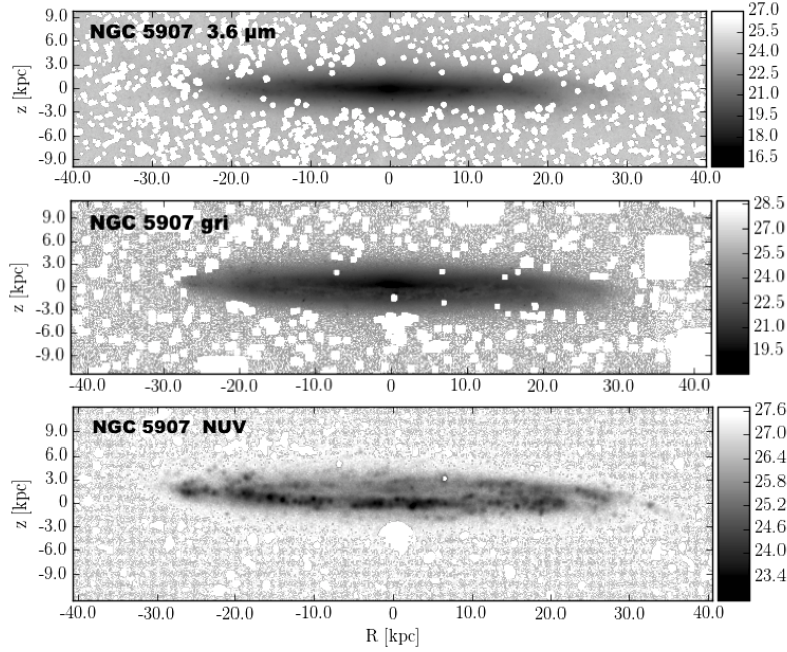


Figure 2. Masked images of NGC 5907 in the three wavelength ranges. The greyscale bar is in surface brightness units (mag arcsec^{-2}).

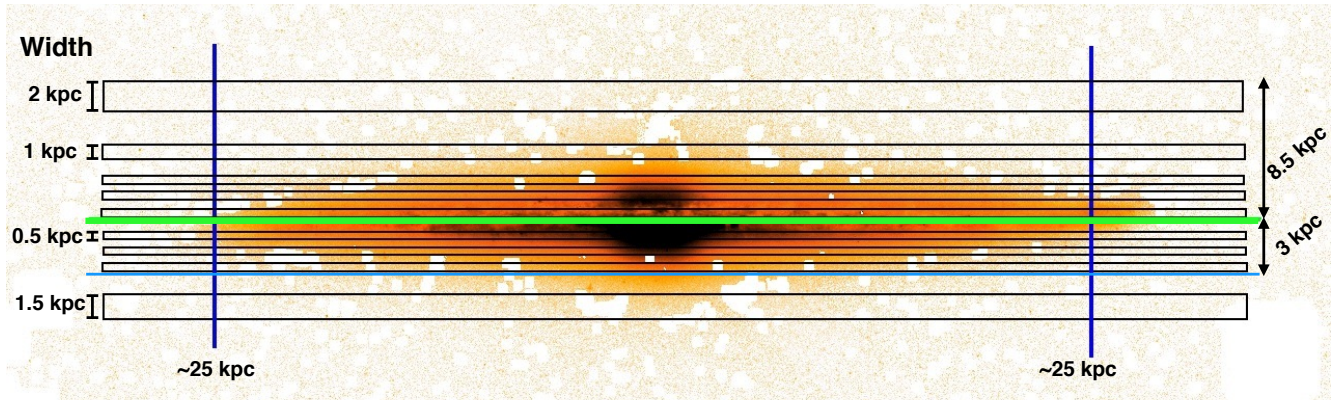


Figure 3. Image of NGC 4565 in the SDSS *gri* combined band. The green horizontal line covers the region along which we obtain the galaxy mid-plane radial surface brightness profile. The black rectangles show the locations where the radial surface brightness profiles above and below the galaxy mid-plane were extracted. The numbers on the left are the widths of each profile. The numbers on the right are (1) the highest altitude we reach (8.5 kpc) and (2) the height up to where we are able to detect the truncation (3 kpc) which is indicated with the horizontal blue line. The vertical dark blue lines point out a radial distance of ~ 25 kpc from the centre of the galaxy. The truncation for this galaxy is located at $\sim 26.4 \pm 0.4$ kpc.

pending on its apparent size and distance. The methodology followed to obtain the profiles is the same for all the wavelength ranges. The first step was to rotate the masked and sky-subtracted galaxy image in order to have horizontal major axes.

To obtain the radial surface brightness profiles, we started with a central profile in the galactic plane using a slit of 0.5 kpc width (see Fig. 3). We calculated the right- and left- band side surface brightness profiles separately, by

dividing the slit into radial logarithmic scale bins, from the centre of the galaxy to the outer regions. The logarithmic bins allow us to increase the signal-to-noise ratio (S/N) in the outskirts. For each bin, we calculated the surface brightness correcting by A_λ , the Galactic extinction coefficient at each wavelength, presented as the total absorption in magnitudes in the NED. The final surface brightness profile was obtained by averaging the left and right radial logarithmic bins at the same distance from the centre of the galaxy. De-

spite small asymmetries in the radial direction, we combine the two sides to explore the surface brightness profiles down to very faint levels (below $\mu \sim 27.0$ mag arcsec $^{-2}$).

After producing the central radial profile, we obtained the *shifted* radial surface brightness profiles at a given height above and below the galaxy mid-plane. We proceed in a similar manner to the mid-plane profile, but averaging the right and left radial logarithmic bins of the profile above and below the galaxy mid-plane. The first *shifted* radial surface brightness profile is obtained at $|z| = 0.5$ kpc above and below the galaxy mid-plane with a height (vertical box) also equal to 0.5 kpc. Then, by repeating the same procedure we go up/down in steps in height of 0.5 kpc up to where we start to lose S/N. We consider low S/N when the mean size of the error bars is larger than the intrinsic oscillations in the profile due to the galaxy structure (i.e., spiral arms, regions of star formation, etc.), and we recover the S/N by increasing the vertical box height. As our two galaxies are different in terms of apparent size and distance, the steps in height above (and below) the mid-plane of the galaxy were as follows (see also Fig. 3): for NGC 4565, boxes with 0.5 kpc height up to 3 kpc, and then steps of 1.0, 1.5 and 2.0 kpc at 4.0, 5.5 and 7.5 kpc altitude, respectively; in the case of NGC 5907, 0.5 kpc boxes up to $|z| = 2.5$ kpc, followed by boxes of 0.7, 1.5 and 2.5 kpc at altitudes of 3.2, 4.7 and 6.7 kpc above the mid-plane, respectively. As we are combining boxes that are above and below the galaxy mid-plane we explored whether there are any significant differences between these two regions of the galaxy (see Appendix B). We do not find any significant difference between the two sides of the galaxies except slightly different surface brightnesses (typically $\Delta\mu_{gri} \sim 0.3$ mag arcsec $^{-2}$ for NGC 4565 and $\Delta\mu_{gri} \sim 0.1$ mag arcsec $^{-2}$ for NGC 5907), expected from the fact that the galaxies are not perfectly edge-on (particularly NGC 5907).

The uncertainties in each bin of the profiles were for all cases defined as

$$\sigma_{\text{bin}}^2 = \sigma_{\text{Pois,bin}}^2 + \sigma_{\text{sky,bin}}^2, \quad (1)$$

which is the quadratic sum of the Poissonian error of the bin ($\sigma_{\text{Pois,bin}}$) and its associated sky error value ($\sigma_{\text{sky,bin}}$). The first is the contribution of the Poissonian error in the determination of the signal in each bin of the profile

$$\sigma_{\text{Pois,bin}} = \text{RMS}(\bar{I}_{\text{bin}} - I_{\text{pix}}) / \sqrt{N_{\text{bin}}}, \quad (2)$$

where I_{pix} is the intensity value of a given pixel inside the bin; \bar{I}_{bin} is the mean intensity value of all the pixels in the bin; RMS is the root mean square of the expression in brackets; and N_{bin} is the number of pixels inside the bin area. The second source of error is the uncertainty in the determination of the sky due to fluctuations at the bin area scale. It can be written as

$$\sigma_{\text{sky,bin}} = \text{RMS}_{\text{sky}} / \sqrt{N_{\text{bin}}}, \quad (3)$$

where RMS_{sky} is the root mean square across the whole image. This quantity was determined over three well-distributed and different background regions of $\sim 200 \times 200$ arcsec in the masked image. We made a Bayesian estimate of the RMS per pixel and the confidence

in the mean for each region by using the Python package `scipy.stats.bayes_mvs` (Oliphant 2006). The uncertainty of the RMS was based on the average confidence limit for the mean.

The last part of this process was to determine the position of the truncation, that we define as the sharp edge of a highly-inclined galaxy. We consider that the slope changes at the position of the intersection between the prolongations of two exponential components in a surface brightness profile. For an unbiased measurement of the truncation radius, we followed the steps of Pohlen & Trujillo (2006, their Sect. 4.2). The scale lengths of the exponential profiles before and after the truncation for each galaxy and the various wavelengths and heights above/below the galaxies mid-plane are shown in Tables 2 and 3. The derived truncation radii are almost always consistent with those derived by eye.

3.4 The effect of the PSF on the surface brightness profiles

Before starting the analysis of our findings we need to explore whether the effect of the point spread function (PSF) can alter the location of the truncation. Although this may appear unlikely along the mid-plane of the galaxies, it is worth exploring whether any potential truncation feature above the mid-plane could be the result of a PSF effect. Another issue to explore is whether the addition of extra light by the PSF in the outer regions of the galaxies (beyond the mid-plane) can affect the location of this feature high above the plane.

The PSF effect is stronger in edge-on than in face-on galaxies (e.g., de Jong 2008; Sandin 2014, 2015) due to the departure from circular symmetry in the edge-on configuration (see a quantification of the effect of the ellipticity on the PSF effect in Trujillo et al. 2001a,b). This has been explored in previous works (e.g., Zibetti et al. 2004; Sandin 2014; Trujillo & Fliri 2016; Peters et al. 2017; Comerón et al. 2018) that showed that the properties of stellar haloes and faint outskirts of galactic discs can be influenced significantly by the wings of the PSF.

To check how the faint wings of the PSF are affecting our measurements, we used an extended and deep SDSS *r*-band PSF ($R = 13.2$ arcmin), built by combining very bright (saturated) and fainter stars (following the procedure of Fliri & Trujillo 2016). We then used IMFIT (Erwin 2015) to perform a 2D fit of a truncated exponential disc for each galaxy, producing PSF-convolved and PSF-deconvolved models of the optical data. We made a two-disc fit (thin and thick disc) with a bulge and a bar component (the latter only for NGC 4565) according to the morphological classification showed in Table 1 to properly reproduce both galaxies. In both cases, we needed a thin disc truncated at the same distance as the data and a pure exponential thick disc. As the dust content is important in the optical (although much less than in UV, see Fig. 2), the central part of the images (i.e., the dust lanes) was masked so the models were determined by extrapolating the analytical functions from the disc regions where the dust is not visible. The 2D fit uses a minimization method based on the Levenberg-Marquardt least-squares algorithm (Moré 1978). Fig. 1 shows how our galaxy images are affected by removing the PSF, mainly

Table 2. Scale lengths in kiloparsecs of the exponential profile fits on both sides of the truncation for NGC 4565. For each height $|z|$ and each wavelength range, we give the numerical value of the exponential fit before and after the truncation radius (h_{bef} and h_{aft}).

$ z $	NUV		SDSS- <i>gri</i>		3.6 μm	
	h_{bef}	h_{aft}	h_{bef}	h_{aft}	h_{bef}	h_{aft}
0.0	-14.8 ± 0.5	1.2 ± 0.2	8.9 ± 0.3	1.7 ± 0.2	4.7 ± 0.2	1.5 ± 0.2
0.5	-84.8 ± 0.5	1.3 ± 0.2	8.3 ± 0.2	2.0 ± 0.2	4.8 ± 0.2	2.0 ± 0.2
1.0	22.5 ± 0.3	2.1 ± 0.3	7.5 ± 0.3	3.0 ± 0.2	5.4 ± 0.3	2.5 ± 0.2
1.5	19.3 ± 0.4	3.1 ± 0.2	7.3 ± 0.2	3.8 ± 0.3	6.0 ± 0.4	3.0 ± 0.2
2.0	17.8 ± 0.3	4.1 ± 0.3	7.6 ± 0.2	4.0 ± 0.2	6.5 ± 0.3	4.1 ± 0.3
2.5	54.7 ± 0.5	6.6 ± 0.3	8.3 ± 0.4	4.8 ± 0.2	7.2 ± 0.4	3.3 ± 0.3
3.0	40.3 ± 0.5	5.1 ± 0.4	9.1 ± 0.4	5.0 ± 0.3	7.3 ± 0.4	3.7 ± 0.3

Table 3. As in Table 2, but for NGC 5907.

$ z $	NUV		SDSS- <i>gri</i>		3.6 μm	
	h_{bef}	h_{aft}	h_{bef}	h_{aft}	h_{bef}	h_{aft}
0.0	-147.1 ± 0.5	1.5 ± 0.1	6.1 ± 0.2	1.5 ± 0.2	3.6 ± 0.2	1.8 ± 0.1
0.5	20.3 ± 0.5	1.3 ± 0.2	5.8 ± 0.2	1.6 ± 0.2	3.8 ± 0.2	2.0 ± 0.2
1.0	6.8 ± 0.2	2.2 ± 0.2	5.5 ± 0.2	1.7 ± 0.2	4.2 ± 0.3	2.2 ± 0.2
1.5	7.8 ± 0.2	2.1 ± 0.2	5.7 ± 0.3	2.0 ± 0.2	5.1 ± 0.3	2.6 ± 0.2
2.0	11.3 ± 0.4	2.3 ± 0.2	7.5 ± 0.3	2.6 ± 0.3	6.3 ± 0.3	3.2 ± 0.3
2.5	12.6 ± 0.4	3.6 ± 0.3	9.9 ± 0.4	2.1 ± 0.2	7.2 ± 0.4	3.6 ± 0.3
3.2	16.0 ± 0.5	5.6 ± 0.3	9.5 ± 0.4	2.0 ± 0.3	8.0 ± 0.4	4.8 ± 0.4

along the minor axis of both galaxies, where the scattered light is redistributed towards the inner parts.

In order to quantify the effect of the PSF on the surface brightness profiles, we extract the surface brightness profiles from the deconvolved images following exactly the same slit configurations as in the original dataset. Fig. 4 shows that the position of the truncation is not affected by the PSF: its value is exactly the same as in the original data (see Sect. 4). In Fig. 4 we also see the truncation up to $z = 3$ kpc, but it is not more prominent than in the data (see details in Figs. A4 and A8). Thus, the truncation position is not affected by the PSF in terms of the height above the galaxy mid-plane where it is detectable, nor in terms of its visibility.

We have explicitly checked the effect of the PSF only on the optical bands as there we have the largest and deepest, and thus most reliable, PSF available (dynamical range of ~ 20 mag and $R = 13.2$ arcmin). Furthermore, the depth of the optical data is similar to IR or NUV (the latter is deeper but with poorer S/N) and any PSF effects will therefore not be much more pronounced in other wavelength than in the optical. As the position of the truncation is independent of wavelength (which implies different telescopes and cameras with both different PSFs and spatial resolutions) and we do not see a large PSF effect in the *r*-filter, we assume that the effect of the PSF is also negligible in the other bands.

To check the possible effect of the PSF in more detail, we considered a truncated infinitely thin disc (i.e., with a vertical scale height equal to zero), which we modelled according to the size scales in our galaxy sample. In this situation, the scattered light thickens the disc but it does so more effectively in the central parts than in the outskirts. As a result, we see that a decline in the surface brightness profile (which resembles a "truncation"-like feature) occurs at increasingly shorter distances from the centre as we move

vertically away from the mid-plane. At a vertical distance of 0.5 kpc, the radial position of this "truncation"-like feature is ~ 2 kpc closer than in the mid plane (where it occurs at $R \sim 26$ kpc), while at a height of 3 kpc it is located at $R \sim 10$ kpc.

While this simple test confirms what is expected, namely that a thin disk model gets thicker after convolving it with a PSF, it produces a result that is very different from what we observe: that the truncation above the mid-plane in real galaxies is at the same radial location at all heights. This test thus strengthens our conclusions that the measured surface brightness at the truncation up to 3 kpc is not dominated by the bright emission coming from the galaxy's mid-plane, that this feature is thus not a PSF artifact, and that the location of the truncation is essentially unaffected by scattered light.

4 RESULTS

4.1 Truncations are more prominent in NUV than in IR

In Fig. 5 we plot the radial surface brightness profiles along the mid-plane of NGC 4565 and NGC 5907 in our three wavelength ranges: *GALEX* NUV, SDSS *gri* combined band and *Spitzer* 3.6 μm . The profiles were obtained as described in Sect. 3.3, where the slit width is 0.5 kpc and the radial bin size changes logarithmically.

In both galaxies, a truncation is clearly observed. The change in slope between the inner region of the disc ($R < R_{\text{trun}}$) and the outer region ($R > R_{\text{trun}}$) is more prominent in bluer bands, and the truncation is most prominent in the NUV band. It is least pronounced, but still clearly present, in the IR. The main difference in the shape of the surface

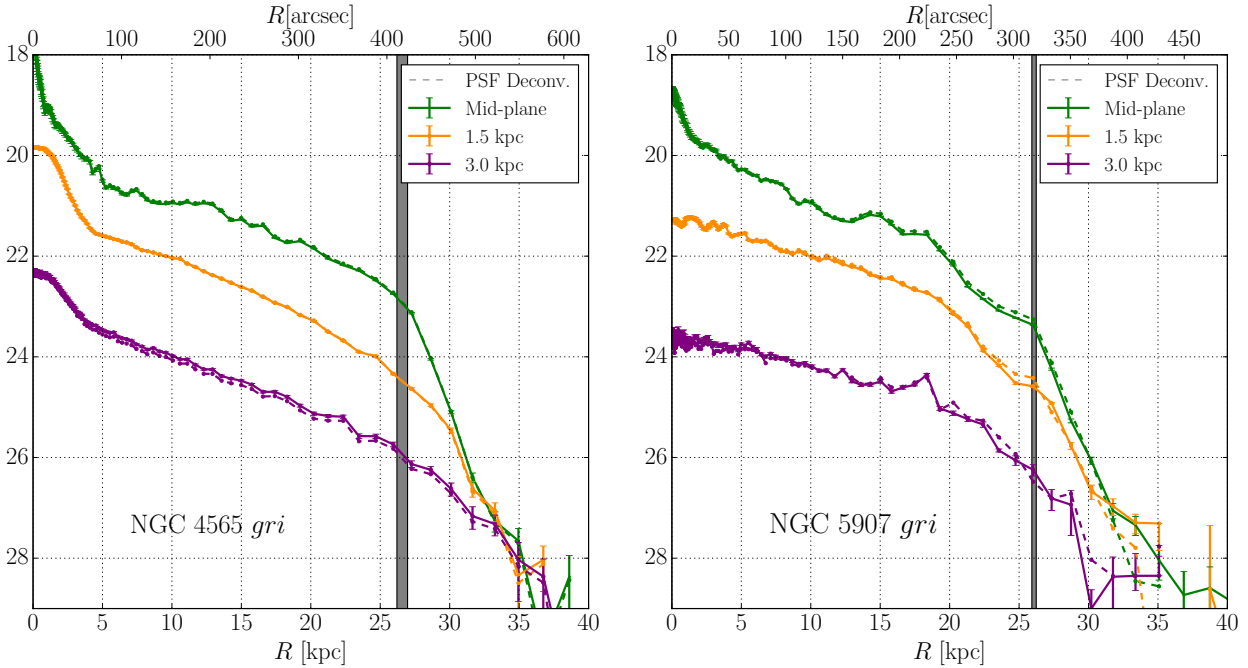


Figure 4. Radial surface brightness profiles for each galaxy at different heights above/below the galaxy mid-plane in the SDSS *gri* combined band for NGC 4565 (left) and NGC 5907 (right). In both panels, the solid curves are radial surface brightness profiles obtained from the observed data along the galaxy mid-plane (green), at a height of 1.5 kpc (yellow) and at a height of 3.0 kpc (violet). The dashed curves represent the same radial surface brightness profiles but for the PSF-deconvolved model of each galaxy at the corresponding location. The vertical boxes of all the profiles are 0.5 kpc wide. The vertical dark grey region represents the mean position of the truncation for all the heights in the SDSS *gri* combined band, plus/minus the standard deviation of that distribution of truncation positions.

brightness profiles is in the flux inside the truncation. Dust in this region severely affects the NUV and to a much lesser degree, the optical profile, producing a much flatter distribution than in the NIR regime (see a review of dust extinction in Mathis 1990).

Figure 5 shows that the stellar mass density (traced by the IR band) in both galaxies has a peak near the centre because of the bulge (more prominent in NGC 4565), decreases slowly until the truncation, and then falls. If we assume the difference between the IR and optical profiles to be predominantly due to dust, we deduce that the amount of dust along the radial direction is such that (up to 10 kpc) it barely affects the slope of the optical profile (particularly in the case of NGC 5907) compared to the stellar mass density profile provided by the IR band⁵, and then it diminishes further until the position of the truncation. The similar slope after the truncation for all bands (see Tables 2 and 3) suggests that there is essentially no dust in that regions, and that the star formation rate (SFR) after the truncation (if anything) is low. Finally, in the NUV band we see that the discs are strongly affected by dust extinction (see also Fig. 2, lower panel) so the distribution is mainly flat with some fluctuations due to either star formation activity peaks or less dust extinction up to the truncation position, for both galaxies. Beyond there, the profiles bend over sharply.

⁵ See the approximately constant *gri*- $3.6\mu\text{m}$ colour of ~ 2 mag inside 10 kpc in both galaxies in Fig. 7.

4.2 Radial SB profiles: truncation position is independent of colour

Figure 6 shows another noteworthy feature in common between the two galaxies: the radial location of the truncation is the same (within the uncertainties) in all three wavelength ranges, NUV (*GALEX*), SDSS *gri* combined band, and IRAC/*Spitzer* $3.6\mu\text{m}$ (Tables 4 and 5). We obtain a mean value for the three wavelengths at the galaxies mid-plane of 26.7 ± 0.4 kpc for NGC 4565 (26.3 ± 0.4 kpc for NUV, 27.0 ± 0.4 kpc in optical, and 26.9 ± 0.4 kpc in NIR), and of 26.2 ± 0.2 kpc for NGC 5907 (26.0 ± 0.2 kpc in NUV, 26.0 ± 0.1 kpc in optical and 26.6 ± 0.2 kpc for the NIR), although these values in physical units are affected by uncertainties in the distance (see Sect. 2 and Table 1). The independence of the location of the truncation on wavelength suggests that the truncation is a robust feature of the galaxies. This is because the truncation is observed in profiles as different as the one that traces the stellar mass density (i.e., $3.6\mu\text{m}$) and the one connected with star formation activity and dust (i.e., NUV). As we will explore later, this makes the truncation into an ideal tool both to measure the sizes of the discs and to explore the ongoing growth of the galaxies.

Interestingly, the surface brightness and the radial position of the truncations are very similar in both objects (i.e., $\mu_{3.6\mu\text{m}} \sim 23$ mag arcsec⁻² and $R_{\text{trun}} \sim 26.5$ kpc). Although we do not know whether this is just by chance or physically connected to the fact that our two galaxies have the same maximum rotational velocity (i.e., ~ 230 km s⁻¹).

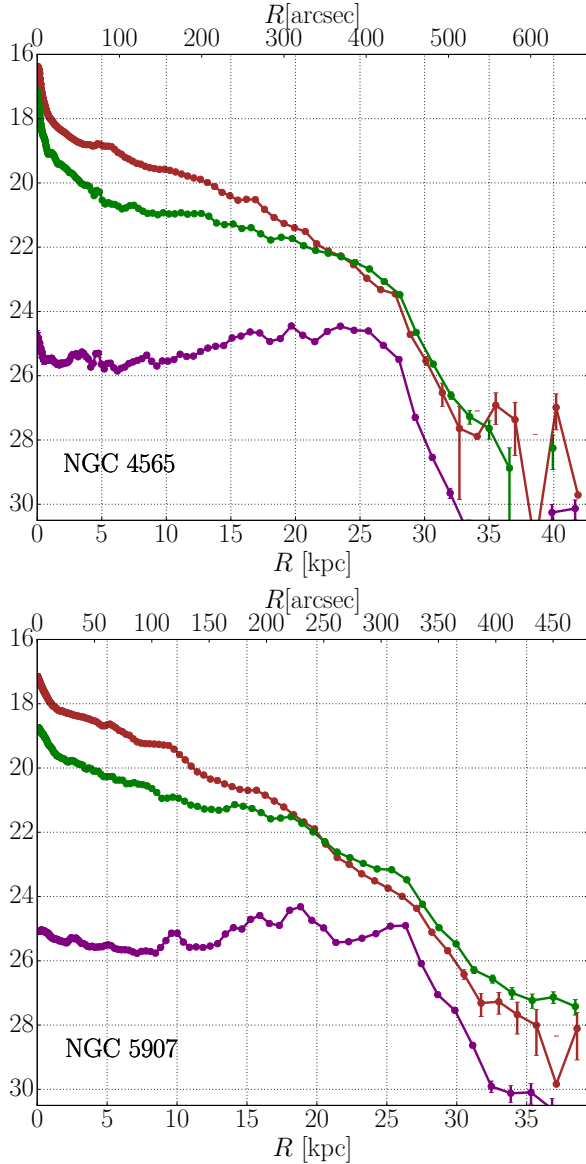


Figure 5. Surface brightness profiles along the disc mid-plane of NGC 4565 (up) and NGC 5907 (down) in the three wavelength ranges studied. In each panel, the three curves correspond, from top to bottom, to NIR (red), optical (green), and UV (purple).

4.3 Comparison with previous studies

NGC 4565 and NGC 5907 were the first galaxies in which a truncation was detected and analysed via surface photometry, from photographic plates (van der Kruit 1979; van der Kruit & Searle 1981a,b). They defined the truncation location as a cut-off radius, R_{\max} , just after a sharp cut-off with an exponential folding of $\lesssim 1$ kpc (see Figs. 5 and 11 from van der Kruit & Searle 1981a). Their values for R_{\max} were 32.6 kpc for NGC 4565 (assumed distance 10 Mpc) and 29.6 kpc for NGC 5907 (for a distance modulus of 11 Mpc). These values were later confirmed with excellent precision using CCD photometry by Morrison et al. (1994) for NGC 5907, and by Wu et al. (2002) for NGC 4565. There is also good agreement with our results if we consider the discrepancies in the truncation (we set the truncation posi-

Table 4. Radial positions of the truncation in kpc at each height $|z|$, and at each wavelength for NGC 4565. The last column shows the mean values at each height above/below the galaxy mid-plane $\langle R_{\text{trunc}} \rangle_z$, while the last row shows the average values for each wavelength range $\langle R_{\text{trunc}} \rangle_\lambda$. $\langle R_{\text{trunc}} \rangle_{z,\lambda}$ is the mean truncation position for all $|z|$ and λ .

$ z $	NUV	SDSS- <i>gri</i>	$3.6\mu\text{m}$	$\langle R_{\text{trunc}} \rangle_z$
0.0	26.3 ± 0.4	27.0 ± 0.4	26.9 ± 0.4	26.7 ± 0.4
0.5	26.4 ± 0.3	27.0 ± 0.3	25.8 ± 0.3	26.4 ± 0.3
1.0	25.8 ± 0.4	26.0 ± 0.3	25.9 ± 0.4	25.9 ± 0.4
1.5	25.9 ± 0.4	26.2 ± 0.4	26.1 ± 0.4	26.1 ± 0.4
2.0	26.9 ± 0.4	26.6 ± 0.4	26.3 ± 0.5	26.6 ± 0.4
2.5	25.9 ± 0.5	26.3 ± 0.4	26.8 ± 0.5	26.3 ± 0.5
3.0	26.3 ± 0.5	27.0 ± 0.4	26.3 ± 0.4	26.5 ± 0.4
$\langle R_{\text{trunc}} \rangle_\lambda$	26.2 ± 0.4	26.6 ± 0.4	26.3 ± 0.4	$\langle R_{\text{trunc}} \rangle_{z,\lambda} = 26.4 \pm 0.4$

Table 5. As in Table 4, but for NGC 5907.

$ z $	NUV	SDSS- <i>gri</i>	$3.6\mu\text{m}$	$\langle R_{\text{trunc}} \rangle_z$
0.0	26.0 ± 0.2	26.0 ± 0.1	26.6 ± 0.2	26.2 ± 0.2
0.5	25.9 ± 0.1	26.2 ± 0.1	26.1 ± 0.2	26.1 ± 0.1
1.0	26.7 ± 0.2	26.1 ± 0.2	26.0 ± 0.3	26.3 ± 0.2
1.5	26.0 ± 0.2	26.3 ± 0.1	26.4 ± 0.2	26.3 ± 0.2
2.0	25.9 ± 0.2	25.9 ± 0.1	25.8 ± 0.2	25.9 ± 0.2
2.5	26.0 ± 0.2	26.0 ± 0.2	25.9 ± 0.2	26.0 ± 0.2
3.2	26.2 ± 0.3	25.8 ± 0.2	25.9 ± 0.3	26.0 ± 0.3
$\langle R_{\text{trunc}} \rangle_\lambda$	26.1 ± 0.2	26.1 ± 0.1	26.1 ± 0.2	$\langle R_{\text{trunc}} \rangle_{z,\lambda} = 26.1 \pm 0.2$

tion at the cut-off of the exponential folding), as well as the different distance values.

There is, also good agreement with Martín-Navarro et al. (2012), who obtained surface brightness profiles for 34 highly inclined spiral galaxies from the S⁴G, including NGC 5907. They find that NGC 5907 is a type II galaxy (truncated) with its truncation position located at $R \sim 26$ kpc, in agreement with our result taking into account that their assumed distance to the object (16.3 Mpc) is slightly different from ours (16.9 Mpc).

Comerón et al. (2012, 2018) studied seventy S⁴G edge-on galaxies, and found, from 1D surface brightness profile fitting of NGC 4565 for the whole disc, but also for each component (thin and thick disc) separately, that NGC 4565 is a type II+II galaxy, i.e., with two truncations along the disc. The second truncation (in which we are interested) is located at 431 ± 12 arcsec (27.5 ± 0.8 kpc) for the whole disc fit. This result again agrees with ours, considering the uncertainties and methodologies in each work.

4.4 Truncation position is constant above the mid-plane

In order to study the vertical behaviour of the position of the truncation, we derived radial surface brightness profiles at different altitudes above (and below) the galactic mid-plane in the two galaxies, as explained in Sect. 3.3. In Appendix A, we show the set of surface brightness profiles: Figs. A1, A2

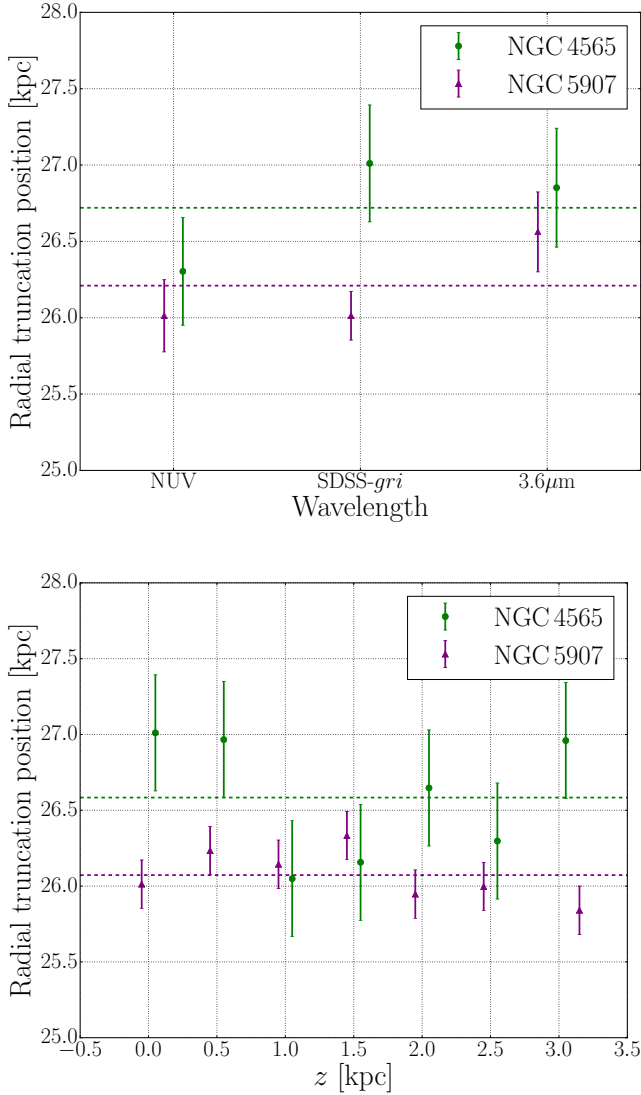


Figure 6. Truncation position at each wavelength, measured from the SB profiles along the disc plane (above) and at different heights in the SDSS *gri* combined band (bottom). In both cases the dashed lines represent the mean value of the points in the corresponding colour.

and A3 show the results for NGC 4565 in the NUV, *gri* and $3.6\mu\text{m}$ bands, respectively, while Figs. A5, A6 and A7 show the results of NGC 5907. The radial positions of the truncations are shown in Tables 4 and 5 for NGC 4565 and NGC 5907, respectively.

In Fig. 6 we summarise this by showing all the positions of the truncation values along the vertical axis in the case of the SDSS *gri* combined band, for both galaxies. The position of the truncation in NGC 4565 is practically constant up to a height of $z \sim 3$ kpc. Above that value, we are unable to explore the truncation and the profiles become compatible with pure exponentials because of the poor S/N. For NGC 5907 we observe the same behaviour, but up to $z \sim 3.2$ kpc. In Appendix A we show that the position of the truncation is roughly the same for the whole wavelength range, up to those altitudes, in both galaxies. It is

important to note that the truncation is always sharpest in the mid-plane and becomes less prominent at larger heights. The average truncation values for all the heights (indicated in Tables 4 and 5 and in Fig. 6 with dashed lines for the optical) are: 26.2 ± 0.4 kpc (NUV), 26.6 ± 0.4 kpc (optical) and 26.3 ± 0.4 kpc (NIR) for NGC 4565 and 26.1 ± 0.2 kpc (NUV), 26.1 ± 0.1 kpc (optical) and 26.1 ± 0.2 kpc (NIR) for NGC 5907.

The independence of the location of the truncation with height has been also found in a previous study: de Jong et al. (2007) showed that the truncation (they call it break) occurs at the same radius independent of the height above the disc up to $z \sim 1.5$ kpc in the low-mass ($v_{\text{rot}} = 98 \text{ km s}^{-1}$; $M_{\text{abs,B}} = -18.4$) edge-on galaxy NGC 4244. This study is based on resolved stellar populations of NGC 4244 by counting stars in both the F606W and F814W bands of the *HST* Advanced Camera for Surveys (ACS). They found that the truncation is sharpest in the mid-plane and nearly disappears at large heights, also in concordance with our results.

In further agreement, Comerón et al. (2012, 2018) found that beyond 3 kpc above the mid-plane, the surface brightness profiles of NGC 4565 do not show any evidence for truncation. In particular, they explored the region from $z \sim 42$ arcsec (2.7 kpc) up to $z \sim 110$ arcsec (7.0 kpc) above the galaxy mid-plane.

Our truncation position values are affected by the spatial resolution of the surface brightness profiles. In NGC 4565, the corresponding surface brightness profile width is equal to 0.5 kpc. In the case of NGC 5907, as its absolute magnitude is similar to NGC 4565 but the distance to the object is higher (see Table 1), the S/N is lower at such altitudes. Consequently, the last profile where we detect the truncation is 0.7 kpc wide. A more conservative statement would thus be that the location of the truncation is the same at all heights up to $z \sim 3$ kpc in both galaxies. Above 3 kpc, this feature is not visible, either (1) because it is where the truncation actually ends and/or (2) the light coming from the thick disc or from the stellar halo outshines the thin disc.

Finally, we stress again that the location of the truncation as visible up to 3 kpc in both galaxies occurs at a similar position. As previously stated, this may either be a consequence of the similar characteristics of the galaxies or simply a coincidence.

4.5 Radial colour profiles

From the radial surface brightness profiles in the three wavelength ranges, we can obtain radial colour profiles. In Fig. 7 we show the *gri*- $3.6\mu\text{m}$ and the NUV-*gri* radial colour profiles for both galaxies along the mid-plane, at 1.5 kpc and at 3 kpc height above/below it. The colours are similar (though bluer in the mid-plane) at the truncation radii for the three altitudes in all cases. Inward of the truncation, the colours show a negative gradient (less clearly for NUV-*gri* in NGC 5907) with a very similar behaviour in the radial profiles at 1.5 kpc and 3 kpc height above/below the mid-plane. The mid-plane profiles are strongly affected by dust, mainly in the inner parts of both galaxies. Beyond the truncation, in the NUV-*gri* mid-plane colour, we can observe an

increase in the colour values for the two galaxies⁶. This U shape around the truncation resembles the behaviour found at the break position in previous works (see e.g., [Azzollini et al. 2008a](#); [Bakos et al. 2008](#)). We will take advantage of this feature below to explore the ongoing growth of these galaxies.

4.6 The vertical extent of the thin disc

Our analysis of the surface brightness profiles above the galaxies mid-plane shows that it is possible to identify the truncation up to at least 3 kpc above/below the disc plane. Moreover, the location of the truncation, within the uncertainty in determining this position, is the same independently of the altitude above the disc. It is difficult to understand this without invoking a similar physical origin for the truncation in both the galactic plane and at higher altitudes. The obvious conclusion is then that the thin disc extends up to at least 3 kpc in height. Thus, we can use the maximum height where the truncation has been identified to provide a lower limit to the vertical extent of the thin disc.

The above result does not imply that there is no need for a thick disc in our two galaxies - our result only suggests that the brightness of any thick disc component is not enough to outshine the truncation feature from the thin disc up to at least 3 kpc height. In this sense, we can make a direct comparison of our results with those of [Comerón et al. \(2018\)](#), who found that the ratio of thick to thin disc mass is a declining function of the total mass of the galaxy as measured by the circular maximum velocity. In the galaxy we have in common, NGC 4565, [Comerón et al. \(2018\)](#) quote a mass ratio between the two disc components of 14%. In addition, they provide the surface brightness profiles of both the thin and thick component (see their Appendix). At the location of the truncation, they report $\Sigma_T(0)/\Sigma_t(0)=0.04$, and scale heights $h_t=7.1$ arcsec (0.45 kpc) and $h_T=49.3$ arcsec (3.15 kpc) for the thin and thick discs, respectively. If we assume an exponential decay for both disc components in the vertical direction: $\Sigma_t(z) = \Sigma_t(0) \times \exp(-z/h_t)$ (thin disc) and $\Sigma_T(z) = \Sigma_T(0) \times \exp(-z/h_T)$ (thick disc), these numbers imply that the thick disc starts to dominate the light of the thin disc at $z = 1.7$ kpc. However, making reasonable assumptions on the dilution of the thin disc truncation by thick disc light (e.g., the thin disc 10 times fainter than the thick disc), we can estimate that the truncation can be observed up to $z \sim 2.9$ kpc, in very nice agreement with our observed result that we detect the truncation of the thin disc at altitudes as high as 3 kpc. In future work, we will use deeper data (with better S/N) of NGC 4565 to investigate whether the truncation can be detected at even larger distances above the mid-plane.

5 THE ONGOING GROWTH OF GALACTIC DISCS

In this Section we will discuss two methods to derive a consistent measure of the ongoing growth of galactic discs. In

⁶ There is a hint that the same behaviour could also happen in the *gri* - 3.6 μ m colour, although the trend is not so obvious as in the NUV - *gri* colour.

the first, we will use the location of the truncation at different heights above the mid-plane. The second method analyses the shape of the radial colour profiles beyond the truncation.

5.1 First approach: offsets in the location of the truncation at different heights

Stars are subject to migrations both in the radial and vertical directions (see for a review [Sellwood 2014](#); [Debattista et al. 2017](#)). Stars currently being formed in the mid-plane at the truncation position will take some time to reach a given height above the mid-plane of the galaxy. For this reason, considering an inside-out propagation of the star formation, the location of the truncation at a high location should be closer to the galactic centre than that in the mid-plane. We illustrate this with a cartoon in Fig. 8.

We call v_{growth} the speed with which the truncation moves radially outwards in the mid-plane. Over an amount of time Δt , the position of the truncation in the mid-plane moves a radial distance ΔR . As stars born at the truncation in the mid-plane take a time to reach a given height z , we can use the different position of the truncation at height z compared to the mid-plane to measure the speed of galaxy growth. The key element is then to know how much time it takes a typical star to reach a certain height z at a given radial distance R . Once this is known, v_{growth} will simply be

$$v_{\text{growth}} = \frac{\Delta R}{\Delta t}. \quad (4)$$

In order to estimate v_{growth} , we estimate how long it takes for a given star in the disc mid-plane to reach a height of 3 kpc (i.e., we calculate Δt). We use $z = 3$ kpc as this is approximately the maximum height at which we are able to measure the truncation above the mid-plane for both galaxies. To estimate Δt , we calculate the difference in gravitational potential between a star located at a radial position R and $z=0$, and a star at the same radial distance R and $z=3$ kpc. This way, we can estimate the initial vertical velocity v_z that a star needs to reach a height z starting from the mid-plane v_z .

The gravitational potential for an infinitely thin disc is given by [Toomre \(1963\)](#)

$$\Phi(R, z) = -2\pi G \int dk \exp(-k|z|) J_0(kR) S(k), \quad (5)$$

where $S(k) = \int dR \Sigma(R) R J_0(kR)$ is the Hankel transform of $\Sigma(R)$, and $J_0(kR)$ is the zero-order first-kind Bessel function.

We consider an exponential disc with surface density

$$\Sigma(R) = \frac{\alpha^2 M}{2\pi} e^{-\alpha R}, \quad (6)$$

where M is the total disc mass and α is the inverse of the disc scale length (h). Thus, if we call $\Sigma_0 = \alpha^2 M / 2\pi$, the resulting gravitational potential as a function of R and z is

$$\Phi(R, z) = \frac{-2\pi G \Sigma_0}{\alpha^2} \int_0^\infty dk \frac{J_0(kR) e^{-k|z|}}{[1 + k^2 \alpha^{-2}]^{3/2}}. \quad (7)$$

As our galaxies are similar to the Milky Way, we use for a

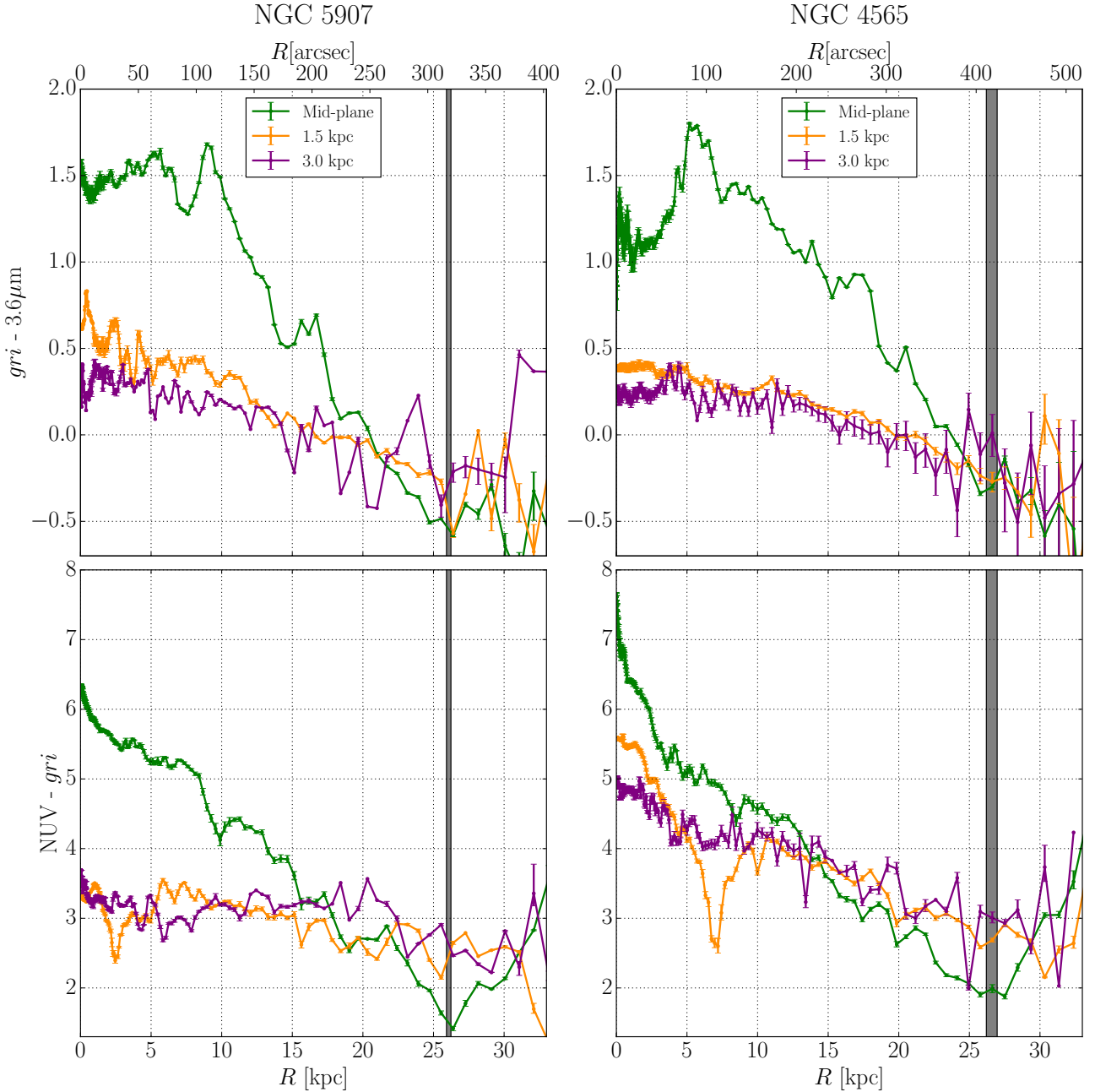


Figure 7. Radial colour profiles for both galaxies along their mid-plane, at 1.5 kpc, and at 3 kpc height (NGC 5907 at left and NGC 4565 at right). The rows show the different colours: $gri - 3.6\mu\text{m}$ in the top row and $\text{NUV} - gri$ in the bottom. The vertical dark grey regions of each galaxy represent the mean position of the truncations for all the heights in the SDSS gri combined band, plus/minus the standard deviation of that distribution of truncation positions: 26.6 ± 0.4 kpc for NGC 4565 and 26.1 ± 0.2 kpc for NGC 5907.

rough estimate of v_z the structural properties of the disc of our Galaxy. In other words, we replace the galaxy’s physical parameters by those of the Milky Way, from [Bland-Hawthorn & Gerhard \(2016\)](#)

$$M = 3.6 \times 10^{10} M_{\odot} \quad ; \quad h = 2.6 \text{ kpc}. \quad (8)$$

We solve numerically the integral of the gravitational potential and we then assume that the corresponding potential energy at $R=26$ kpc and $z=3$ kpc is equal to the kinetic

energy at the same radial distance but at $z=0$ kpc. Hence, taking the values above, we find $v_z = 8.1 \text{ kpc Gyr}^{-1}$ (i.e., $v_z \sim 7.9 \text{ km s}^{-1}$) at $R=26$ kpc.

Once we have the gravitational potential distribution along the disc, the gravitational acceleration at any (R, z) position is given by

$$g(R, z) = -\nabla\Phi(R, z). \quad (9)$$

Having v_z we are now ready to estimate Δt . We divide the

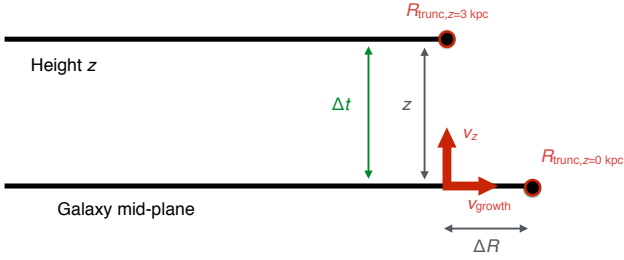


Figure 8. A cartoon illustrating how to use the different vertical locations of the radial position of the truncation to measure the ongoing growth of the galaxies. Stars take a time Δt to reach a certain height z above the galaxy mid-plane. During such time, the location of the truncation in the mid-plane moves a radial distance ΔR . In this particular example, we use $z=3$ kpc to illustrate this idea.

trajectory of the star from $z=0$ to $z=3$ kpc in steps of 0.1 kpc. This simplifies our measurement, as we can assume constant acceleration in such small vertical steps and we can use the motion equations for a particle under uniform acceleration. With the above v_z , the amount of time a star at $R=26$ kpc needs to reach $z=3$ kpc is $t \sim 0.4$ Gyr.

These give us now the possibility to estimate v_{growth} . In reality, as we are unable to measure ΔR with our current uncertainties, we use those uncertainties to provide an upper limit to the maximum growth speed of the discs in our two galaxies. For NGC 4565 we use $\Delta R < 0.25$ kpc and for NGC 5907 $\Delta R < 0.4$ kpc. With such values, the maximum speed for the growth of our galaxies is: $v_{\text{growth}} < 1$ kpc Gyr $^{-1}$ for NGC 4565 and $v_{\text{growth}} < 0.6$ kpc Gyr $^{-1}$ for NGC 5907.

We stress the approximations that we have used in our estimate of v_{growth} . The most relevant one is that we have neglected the effect of the gravitational potential of both the bulge component and the dark matter halo of these galaxies. This is justified as we have only explored the difference in gravitational potential in a region very close to the galactic disc (i.e., $z=3$ kpc) and at a large distance from the center ($R=26$ kpc). At this location, the difference in radial distance between a star in the mid-plane and one at $z=3$ kpc is just 0.2 kpc and the gravitational potential of the bulge is basically the same in both locations. Similarly, assuming a spherical dark matter halo, the small difference in the radial position with respect to the galactic centre implies that the variation of the gravitational potential for such structure is small. Another source of uncertainty in our estimate is the use of the stellar mass and radial scale length of the MW to model these two galaxies. We base this approximation on the fact that their rotational velocities are similar to the one in our own Galaxy.

We now discuss how reasonable the value of v_z is that we have estimated. To do this we use the fact that we know the surface brightness at the location of the truncation, both at $z=0$ and $z=3$ kpc; at $z=0$: $\mu_{3.6\mu\text{m}} \sim 23$ mag arcsec $^{-2}$, and at $z=3$ kpc: $\mu_{3.6\mu\text{m}} \sim 26$ mag arcsec $^{-2}$. Consequently, the difference in stellar mass density, assuming a similar M/L ratio for both locations, is a factor of 16. In other words, stars are 16 times more abundant in the disc mid-plane than at 3 kpc height at the location of the truncation. We assume now that the vertical velocity distribution of stars at the lo-

cation of the truncation is Gaussian. Under this hypothesis, the vertical stellar distribution would be also well approximated by a Gaussian distribution with a width similar to the vertical velocity distribution one. As the density of stars at 3 kpc is a factor of 16 smaller than at $z=0$ kpc, assuming that the stellar vertical density declines as a gaussian distribution 3 kpc will then correspond to a height of $\sim 2.4\sigma$ over the plane. Now, it is straightforward to estimate the vertical velocity distribution σ_z knowing that at 3 kpc, the aforementioned value of $v_z \sim 7.6$ km s $^{-1}$ corresponds to $2.4\sigma_z$. Consequently, $\sigma_z \sim 3.4$ km s $^{-1}$. Unfortunately, there are no measurements of the vertical velocity dispersion of the stars at radial distances as large as $R=26$ kpc. We can only compare this number with the typical velocity dispersion of the thin disc at the radial location of the Sun ($R=8.2 \pm 0.1$ kpc): $\sigma_z^t = 25 \pm 5$ km s $^{-1}$ (Bland-Hawthorn & Gerhard 2016). As expected, the estimated velocity dispersion at $R=26$ kpc is significantly smaller than at $R=8$ kpc. As the velocity dispersion is expected to decrease as the square root of the mass density, the mass density at the Solar position should then be $\sim (25/3.4)^2 \sim 54$ times larger than at the truncation. As the local mass surface density at the Solar position is $70 \pm 5 M_{\odot} \text{pc}^{-2}$ (Bland-Hawthorn & Gerhard 2016), our prediction is that the local mass surface density at the truncation should be $\sim 1.3 M_{\odot} \text{pc}^{-2}$. We can check whether such value is consistent with the stellar mass densities one can derive from the stellar population properties at the truncation position.

We have used two different methods for estimating the stellar mass density based on the stellar population properties. The first one uses the stellar population models in Vazdekis et al. (2016), assuming a bimodal initial mass function of slope 1.3 (similar to the one of Kroupa, Kroupa 2001) and Solar metallicity. We extract the M/L ratio at $\mu_{3.6\mu\text{m}}$ for the age obtained from the NUV-*gri* colour profile (note that the M/L at $\mu_{3.6\mu\text{m}}$ is almost independent of metallicity; see Figs. 13 and 14 in Röck et al. 2015) for each galaxy. From this and the surface brightness at $3.6\mu\text{m}$ corrected for inclination (which is around 2 mag; Martín-Navarro et al. 2014) we obtain the stellar mass density at the position of the truncation. Alternatively, we can also use the *g-r* colours as well as the surface brightness in *r*-band (corrected for inclination) at the truncation and derive a M/L using the prescription by ?. Using both methods we estimate the stellar mass density at the truncation position to be within the following ranges: 1.4-2.4 $M_{\odot} \text{pc}^{-2}$ for NGC 4565, and 0.4-1.4 $M_{\odot} \text{pc}^{-2}$ for NGC 5907. These numbers are consistent with a local mass surface density at the truncation of $\sim 1.3 M_{\odot} \text{pc}^{-2}$, even though we are using simple approximations.

5.2 Second approach: the shape of the radial colour profile beyond the truncation

A completely independent way to measure the growth speed of galaxies is by exploring the shape of the radial colour profile beyond the truncation. The main assumption that we make in this approach is that there is negligible new star formation beyond the truncation. This seems to be a very good approximation, considering the sharp decline in all the surface brightness profiles, particularly in the NUV, after the truncation. If our hypothesis is correct then we can interpret the gradual reddening colour of the stars beyond the trun-

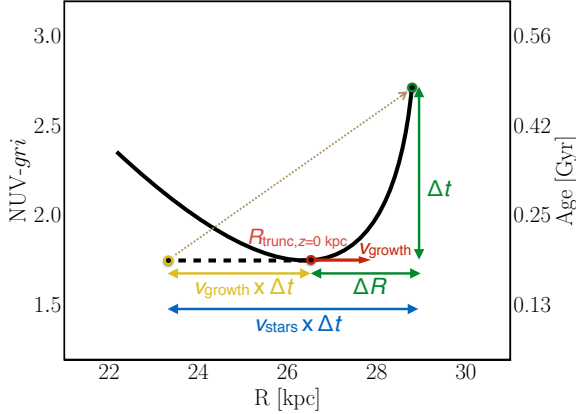


Figure 9. A cartoon illustrating how to use the shape of the radial colour profile beyond the truncation to estimate the growth speed v_{growth} of a disc. The observables in the radial colour profile beyond the truncation are Δt and ΔR . In this particular example we use the colour NUV- r (vertical left axis) as a proxy to measure the interval of time (vertical right axis). The yellow dot indicates the birth location of a star in the colour-radial distance plane. The green dot is the current position of the star born at the yellow dot location. The red dot is the position of the truncation.

cation as purely driven by the passive aging of their stellar populations. We also assume that beyond the truncation the dust obscuration is not playing any role, in agreement with the idea that there is no star formation beyond this point.

In order to estimate the growth speed of the disc v_{growth} we follow the scheme presented in Fig. 9 (based on the data from Fig. 10). We use the NUV- r radial colour profile⁷ as a proxy for measuring the time interval Δt . We use this colour as this combination of bands is very sensitive to recent star formation and consequently allows us to measure intervals of time of the order of 100 Myr. In our scheme, stars are born at a radial position R (which coincides with the initial location of the truncation at the beginning of the time interval). After a given time Δt , the stars have moved outwards a radial distance $v_{\text{stars}} \times \Delta t$. At the same time, the truncation has also moved outwards by $v_{\text{growth}} \times \Delta t$. It is then straightforward to show that

$$v_{\text{growth}} = v_{\text{stars}} - \frac{\Delta R}{\Delta t}. \quad (10)$$

The values ΔR and Δt can be inferred directly from the data. The interval Δt is measured using $\Delta(\text{NUV-}gri)$. In Fig. 10 we highlight the location of the truncation region for our two galaxies.

We use the following measurements of colour and radial distance to derive ΔR and Δt . For the galaxy NGC 4565: (27.6 ± 0.2 kpc, 1.9 ± 0.1 mag) and (28.3 ± 0.2 kpc, 2.2 ± 0.2 mag); and for the galaxy NGC 5907: (26.9 ± 0.1 kpc, 1.5 ± 0.2 mag) and (27.4 ± 0.1 kpc, 1.9 ± 0.2 mag), which

⁷ Actually, we use the colour profile NUV- gri to gain S/N in the outer regions of the galaxies. We have confirmed that the combined gri surface brightness profile is equivalent to the r -band to a level below 0.1 mag along the entire profile of the galaxies.

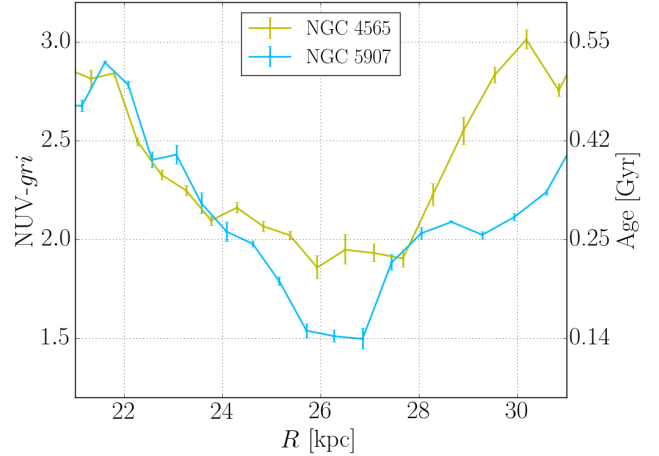


Figure 10. A zoom in to the location of the truncation in the NUV- gri colour versus radial location plane. The right vertical axis shows the age corresponding to the NUV- r colour based on the stellar populations models from Vazdekis et al. (2016).

corresponds to the intervals: $\Delta R = 0.6 \pm 0.2$ kpc and $\Delta t = 0.1 \pm 0.01$ Gyr for NGC 4565; and $\Delta R = 0.6 \pm 0.1$ kpc and $\Delta t = 0.09 \pm 0.01$ Gyr for NGC 5907. The transformation from NUV- gri colour to age has been done using the Vazdekis et al. (2016) models, assuming Solar metallicity and a bimodal initial mass function (as in Sect. 5.1). Consequently, for both galaxies we have $\Delta R / \Delta t \sim 6 \pm 2$ kpc Gyr⁻¹ (i.e. $\sim 6 \pm 2$ km s⁻¹).

As a next step, we need to calculate v_{stars} . Unfortunately, there are no measurements of this value at such locations in galaxies like ours. We can use the ratio of velocity dispersions at the Solar location, $\sigma_R^t / \sigma_z^t = 35/25$ (Bland-Hawthorn & Gerhard 2016), and assume that this ratio is the same at the location of the truncation. This assumption is quite uncertain, but we can use such a value to illustrate the method. If the above assumption is reasonable, and taking $\sigma_z^t \simeq 3.4$ km s⁻¹ from Section 5.1, then the typical velocity dispersion at the radial position of the truncation would be $\sigma_R^t = 7/5 \times \sigma_z^t = 7/5 \times 3.4$ km s⁻¹ ~ 5 km s⁻¹ $\sim v_{\text{stars}}$. This value is very similar to the quantity $\Delta R / \Delta t$ we have estimated above, indicating that v_{growth} should be small (i.e., $v_{\text{growth}} < 0.5$ kpc Gyr⁻¹). We acknowledge that this estimate is strongly dependent on the exact value of v_{stars} used, that is unfortunately not known.

Compared to the approach shown in the previous Section, the colour-based method to measure v_{growth} is much more uncertain and depends strongly on the assumptions we have made. For example, our measurement of Δt is based on the inference of age associated to the colour NUV- gri which depends on the properties of the stellar population model used. As a way to test the robustness of measuring Δt from the colour NUV- gri , we can compare the predictions for such an interval of time based on a completely different stellar population model (Han et al. 2007) that accounts for the binary population. According to this model, NUV- $r = 1.5$ mag corresponds to 0.14 Gyr, NUV- $r = 1.9$ mag to 0.21 Gyr and NUV- $r = 2.2$ mag to 0.28 Gyr, implying $\Delta t = 0.07$ Gyr for

NGC 4565 and $\Delta t=0.07$ Gyr for NGC 5907. These values are similar to the ones inferred using the Vazdekis et al. (2016) model (i.e., ~ 0.1 Gyr). We conclude that, as we have stated before, the weakest point in this approach is the estimate of v_{stars} .

In the Introduction we reported the possibility of a common origin for breaks and truncations by considering the predictions in Roškar et al. (2008a). Their simulations suggest that the U shape in the colour profiles is the result of stellar migration as the stars can gain angular momentum and move outwards, or lose it and move inwards. This is a stochastic movement, both inwards and outwards, where the average displacement scales with $t^{1/2}$ for a stellar population with a given age. Hence, only the oldest stars get to the larger radii which means that the colours become redder when going outwards, but the break radius may not necessarily be growing. In this sense, our growth rate results might be degenerate as the interpretation of a growing disc is not unique. However, it is important to highlight that in Roškar et al. (2008a) the breaks are located at radial distances more than two times smaller than our results. We find the truncation at $R_{\text{trunc}} \sim 26$ kpc, while the simulations of Roškar et al. (2008a) report $R_{\text{break}} \sim 10$ kpc. The corresponding stellar mass density at the position of the break, $R_{\text{break}} \sim 10$ kpc, is $\sim 10 M_{\odot} \text{pc}^{-2}$ (see Fig. 1 in Roškar et al. 2008a), while here the stellar mass densities at the truncation position are $1.4 - 2.4 M_{\odot} \text{pc}^{-2}$ (NGC 4565) and $0.4 - 1.4 M_{\odot} \text{pc}^{-2}$ (NGC 5907). The observational work on type II breaks of Bakos et al. (2008, see their Fig. 1) is in very good agreement with the predictions of Roškar et al. (2008a), which suggests that it is worth exploring whether the features that we are tracing in this work are the same as these in the simulations by Roškar et al. (2008a).

In Fig. 11 we show qualitatively how the shape of the radial colour profile would be in the vicinity of the truncation in terms of the disc growth speed v_{growth} and the stellar migration speed v_{stars} . We see that the radial colour profile beyond the truncation becomes steeper when the disc growth speed is larger than the migration speed of the stars. Otherwise, the slope is smoother. By measuring the slope of the radial colour profile after the position of the truncation, we can thus set an upper limit to the growth speed. Comparing Fig. 11 with Fig. 10, we see that the slope in the colour profiles of our data (Fig. 10) is more similar to the case in that the disc growth speed v_{growth} is lower than the migration speed of the stars v_{stars} (case C in Fig. 11), in agreement with our results.

6 A COMPARISON WITH THE COSMOLOGICAL GROWTH OF DISCS

Although it would be extremely interesting to measure, to the best of our knowledge no one has probed how the radial location of the truncation is moving with cosmic time. The most closely related approach was by Trujillo & Pohlen (2005), later expanded by Azzollini et al. (2008b). In those works, the type II breaks of galaxies were incorrectly called truncations. Nowadays, we know that the type II breaks correspond to a feature in galaxy discs at closer radial distances than the truncations (see a full discussion on this issue in Martín-Navarro et al. 2012). While acknowledging that the

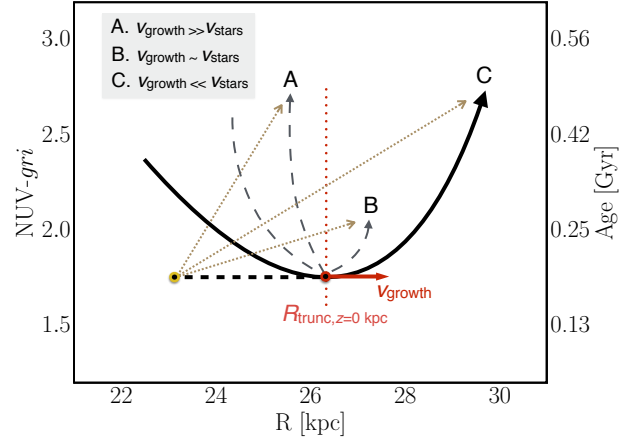


Figure 11. A cartoon illustrating the shape of the radial colour profile beyond the truncation in terms of the disc growth speed v_{growth} and the stellar migration speed v_{stars} . The yellow dot indicates the birth location of a star in the colour-radial distance plane. The red dot is the current position of the truncation. The three dark yellow arrows (square dotted lines) represent the paths of the new-born star, depending on the growth and migration speeds. The star will end up either in position A, B, or C if its migration speed is smaller than, similar to, or greater than the disc growth speed, respectively.

origin of the breaks and the truncation could be different, we can nevertheless use the growth of the discs inferred from the movement of the position of the type II breaks to put our current measurements of the speed of the truncation into a context.

According to Fig. 8 in Azzollini et al. (2008b), present-day MW-like galaxies ($M_{\star} \sim 5 \times 10^{10} M_{\odot}$) would have their break at $R_{\text{break}} \sim 11$ kpc. At redshift ~ 1 , objects with the same stellar mass would typically have $R_{\text{break}} \sim 8$ kpc. However, a galaxy like the MW had a lower stellar mass 8 Gyr ago. This means that we can expect R_{break} to be smaller than 8 kpc for the progenitor of the MW at redshift ~ 1 . Consequently, the 3 kpc increase in the location of the position of the break in the last 8 Gyr must be considered a lower limit for their speed. In other words, the average cosmic speed for the location of the break for MW-like galaxies was $> 0.4 \text{ kpc Gyr}^{-1}$, and probably not larger than 0.5 kpc Gyr^{-1} assuming that the progenitor of the MW at redshift ~ 1 was two times less massive than it is now. In this sense, if the current growth speed of the truncation were comparable with the cosmic growth in the location of the break, we would not expect velocities larger than 0.5 kpc Gyr^{-1} . This number is in nice agreement with our upper limits for the speed of the truncation found above.

7 WHAT IS THE PHYSICAL ORIGIN OF THE TRUNCATION?

7.1 Maximum angular momentum or star formation threshold?

Multiple ideas have been discussed in the literature to understand the origin the truncation of galaxy discs. The two main concepts have been that the position of the truncation reflects the maximum angular momentum of the protogalactic cloud at the moment of collapse (van der Kruit 1987) or, alternatively, that the location of the truncation reflects the location of the disc where there is a threshold in the star formation activity (Kennicutt 1989). In both scenarios, the presence of stars beyond the truncation can be understood if there is a mechanism of radial migration (see for a review Sellwood 2014; Debattista et al. 2017) at work. A direct consequence of radial migration would be that, even if originally the angular momentum distribution of the stars were reflecting that of the protogalaxy, a substantial redistribution of the angular momentum is expected to take place due to secular evolution processes. For example, bars may play an important role in such a redistribution, as suggested by Debattista et al. (2006) and Erwin et al. (2008). Additionally, transient spiral arms cause greater angular momentum changes to stars at co-rotation than to those at the Lindblad resonances (Sellwood & Binney 2002) and can thus move co-rotating stars radially without heating the disc. Roškar et al. (2008b) showed that this mechanism is the one responsible for the largest amounts of redistribution because it is very efficient and can operate on relatively short timescales.

The analysis of the properties of truncations that we have made in this paper can shine some light on the physical processes that are taking place at such locations in galaxies. The first thing to note is that we have detected for the first time a U shaped colour at the location of the truncation. This feature (found previously at the location of breaks in Type II galaxies, Azzollini et al. 2008a; Bakos et al. 2008) is considered to be associated to a star formation threshold followed by a migration of stars to the outer regions (Roškar et al. 2008b,a). It thus seems that the truncation in the two MW-like galaxies we have analysed is closely related to a star formation threshold. It is worth noting that the surface brightness at the position of the truncation is significantly lower than the typical brightness of the breaks in Type II galaxies. In fact, the average surface brightness of the break in the r -band is 22 mag arcsec⁻² for galaxies with the brightness of our objects (see Fig. 9 in Pohlen & Trujillo 2006) whereas here we find for the truncation (after deprojecting the brightness by the effect of the inclination) 25.5 mag arcsec⁻². This corresponds to a factor of ~ 25 less in stellar mass density for the truncation with respect to the break. Using the NUV- gri and $g-r$ colours at the location of the truncation we get a stellar mass density of $\sim 1 - 2 M_{\odot} \text{pc}^{-2}$. This stellar mass density is at the bottom edge for the critical gas density value assumed to trigger the star formation (i.e., $\sim 3 - 10 M_{\odot} \text{pc}^{-2}$; Schaye 2004), which in turn implies that the star formation at this location is quite efficient ($\sim 30\%$).

Both the stellar mass density at the location of the truncation and the U shaped colour profile at this position suggest that the truncation is linked to a star formation threshold. The presence, however, of the truncation up to a height

of $z \sim 3$ kpc, where the density is much lower than in the mid-plane, seems to be difficult to explain as the result of a threshold of star formation at such an altitude. In fact, the characteristic U shape is not observed at high altitudes (see Fig. 7). This indicates that truncations seen at high altitudes may rather be the result of migration of stars from the mid-plane to higher altitudes.

7.2 Dust absorption

Dust absorption along the mid-plane, especially in the NUV and optical bands, might be evaluated as a potential reason for the presence of a truncation as the dust might cause a flatter apparent gradient in the galaxies' mid-plane radial surface brightness profiles than the true stellar surface density gradient. In theory, this could cause the truncation feature to be just an illusion, created by the largest radius with substantial dust content in the mid-plane. The radial colour profiles in Fig. 7 show the clear effect of the dust absorption in the galaxies' mid-planes, mainly in the inner parts. However, the radial colour profiles of NGC 5907 at the mid-plane, at 1.5 kpc, and at 3 kpc converge on a radius of $\sim 15 - 18$ kpc and have similar colours until the truncation position, where the U shape appears in the mid-plane colour profiles. Thus, the dust-free regions (i.e., at high altitudes above/below the galaxy mid-plane) have the same colours than the mid-plane from $\sim 15 - 18$ kpc in this particular case. For NGC 4565, we find a similar behaviour but from $\sim 12 - 15$ kpc for the NUV- gri colour profiles and from ~ 23 kpc for $gri - 3.6\mu\text{m}$. Furthermore, we find that the radial position of the truncation is similar across all wavelengths and up to 3 kpc height above/below the mid-plane of both galaxies (see Sects. 4.2 and 4.4). All these results point to the truncation being a real feature, unaffected by dust absorption.

7.3 Warps

Another possible origin for the truncations (in the mid-plane) is the presence of warps in the discs of galaxies (e.g., van der Kruit 1979; Naeslund & Joersaeter 1997), as one might expect a truncation-like signature at the area where the disc warp begins. Both of the galaxies in our sample have a warp so a proper analysis is necessary. Rupen (1991) reports a warp in the HI emission starting at about 7 arcmin distance from the centre of the galaxy on both sides of NGC 4565. An optical warp that follows the HI warp has been discussed by van der Kruit (1979) and Naeslund & Joersaeter (1997). A warp in the HI gas and in the optical in NGC 5907 has also been reported in several works (e.g., Shang et al. 1998), starting at 5 arcmin radius (see also Florido et al. 1992). Fig. 1 shows how the disc isophotes are bending away from the mid-plane near the end of the bright disc component, suggesting a warp-like shape. In the case of NGC 4565 the warp is more clear in the upper right part of the image although it can be seen in the left side of the galaxy disc towards lower regions (Q2 and Q3, respectively in Fig. C1). For NGC 5907 the warp seems to occur in the opposite way, from the upper left part of the disc towards the lower right region (Q1 and Q4, respectively in Fig. C2). Our observations thus confirm the presence of optical warps at the position of the truncations in the mid-plane.

A potential concern is whether the truncations in the mid-plane could be hidden while observing the galaxy in face-on projection. In order to study this possibility, we have explored whether the position of the truncation continues to be at the same radial location when we explore the galaxy regions with and without the warp. Thus, in Appendix C (Fig. C3), we present an example of the surface brightness profiles at two different heights above/below the mid-plane (0.5 and 2 kpc) in the three wavelength ranges (NUV, *gri* combined band, and $3.6\mu\text{m}$), through the warped and non-warped regions, for both galaxies (indicated in Figs. C1 and C2, for NGC 4565 and NGC 5907, respectively). In these figures, we can see that the presence of a warp barely affects the surface brightness profiles of the galaxies. The only major change is observed in the galaxy NGC 4565 in the NUV profile. There, the presence of a warp pushes the position of the truncation at 2 kpc height towards a larger radial distance compared to the surface brightness profiles closer to the mid-plane. This effect is not seen in the other galaxy, nor in the redder wavelengths.

The results presented here suggest that the warp is populated by very young stars. In the case of NGC 4565 this is confirmed by the stellar population analysis conducted by Radburn-Smith et al. (2014) where they found the warp stellar population to be < 600 Myr old. In this sense, if one were observing the galaxies at moderate inclinations using optical or infrared bands, the truncations will still be clearly observed at the same radial location than in the edge-on case. We conclude that the presence of a warp does not affect our major conclusion that the location of the truncation at different heights is basically at the same position as in the galaxies' mid-plane. In an upcoming paper (C. Martínez-Lombilla et al., in prep.) we will use new ultra-deep imaging of NGC 4565 to address the optical properties of its warp in more detail and relate them to the observed truncation.

7.4 Stars beyond the truncation

We can now consider the number of stars beyond the truncation in the mid-plane of the galaxies. Using the mid-plane $3.6\mu\text{m}$ surface brightness profile (a good proxy for the stellar mass density that is barely affected by the dust) we find fractions of 0.2% (NGC 4565) and 0.1% (NGC 5907). We can make a crude estimate to see whether such an amount of stars is compatible with the idea of radial migration from the region of the truncation to the outer part of the disc. As we have said before, we expect a radial velocity for the stars at the radial position of the truncation of $\sim 6 \pm 2$ kpc Gyr^{-1} . In practical terms this means that the stars produced at the location of the truncation can fill very quickly the outer regions of the galaxies (beyond the truncation). Considering $v_{\text{growth}} < 0.6$ kpc Gyr^{-1} and a typical stellar mass density of $\sim 1 M_{\odot} \text{pc}^{-2}$, the total mass of stars in an annulus around the truncation (i.e., inner radius $R_i = 26$ kpc and outer radius $R_o = 26.5$ kpc) is $\sim 0.8 \times 10^8 M_{\odot}$. This represents, assuming the total stellar mass of a typical MW galaxy of $5 \times 10^{10} M_{\odot}$, a fraction of $\sim 0.15\%$. These crude numbers show that there are enough stars at the location of the truncation to fill the outer parts of the discs, simply by the process of migration.

7.5 Type II breaks

Finally, we consider whether a star formation threshold origin for the truncation may contradict the presence of a profile break in galaxies, that has also been related to star formation activity. One of the most important results by Martín-Navarro et al. (2012) is that, for galaxies with rotational velocities above $v_c > 100$ km s^{-1} (see their Fig. 13), the ratio between the location of the truncation and the break is quite constant, at around 1.8. This could indicate that both features could be linked with different resonances like transient spiral arms (Roškar et al. 2008b). The fact that both features correlate strongly with the rotational velocities of galaxies reinforces this view.

To summarize, our observational results, together with other evidence from the literature, points to a scenario where both the origin and the location of the truncation is directly linked to a threshold in the star formation activity. This threshold is due to the gas density at such a location which ultimately is connected to the angular velocity of rotation at that radial distance in the galaxy. Migration of stars from their birthplace leads both to the truncation observed well above and below the disc mid-plane, and to the small but significant quantity of stars observed beyond the truncation radius.

8 CONCLUSIONS

We have explored the nature of the disc truncations in two edge-on nearby MW-like galaxies: NGC 4565 and NGC 5907. We have used *GALEX*, SDSS and *Spitzer* S⁴G imaging to extract radial surface brightness profiles in and above the mid-planes of the galaxies. We have found the following results:

- Truncations are observed at the same spatial location ($\sim 26 \pm 0.5$ kpc within the spatial uncertainties) at all wavelength ranges (NUV, optical and $3.6 \mu\text{m}$) in both galaxies.
- The truncations are observed at the same spatial location (within the uncertainties) up to a vertical location above the mid-planes of 3 kpc.
- At the location of the truncation, the NUV-*gri* colour radial profile shows the characteristic U shape associated with a star formation threshold, in combination with the migration of stars to the outer regions of the galaxies.
- The stellar mass density at the location of the truncation is $\sim 1 - 2 M_{\odot} \text{pc}^{-2}$. This number is very close to the critical gas density necessary to transform gas into stars of $\sim 3 - 10 M_{\odot} \text{pc}^{-2}$, indicating an efficiency of $\sim 30\%$ for this process at the radial location of the truncation.
- The number of stars in the mid-plane beyond the truncation amounts to 0.1–0.2% of the total stellar mass density of these galaxies. Migration of stars formed inside the truncation radius to the outer regions can explain this number.
- The vertical extent of the truncation as well as the colour properties in the mid-plane beyond the truncation are consistent with an upper limit for the current growth speed for the discs of the galaxies of $0.6 - 1$ kpc Gyr^{-1} .

ACKNOWLEDGEMENTS

We thank Javier Román and Raúl Infante for providing the extended SDSS *r*-band PSF, and Sebastián Comerón for a number of useful suggestions. We acknowledge support from the Spanish Ministry of Economy and Competitiveness (MINECO) under grant numbers AYA2013-41243-P, AYA2016-76219-P and AYA2016-77237-C3-1-P. J.H.K. and I.T.C. acknowledge financial support from the European Union’s Horizon 2020 research and innovation programme under Marie Skłodowska-Curie grant agreement No. 721463 to the SUNDIAL ITN network and from the Fundación BBVA under its 2017 programme of assistance to scientific research groups, for the project “Using machine-learning techniques to drag galaxies from the noise in deep imaging”. J.H.K. thanks the Leverhulme Foundation for the award of a Visiting Professorship at Liverpool John Moores University.

Funding for SDSS-III has been provided by the Alfred P. Sloan Foundation, the Participating Institutions, the National Science Foundation, and the U.S. Department of Energy Office of Science. SDSS-III is managed by the Astrophysical Research Consortium for the Participating Institutions of the SDSS-III Collaboration including the University of Arizona, the Brazilian Participation Group, Brookhaven National Laboratory, University of Cambridge, Carnegie Mellon University, University of Florida, the French Participation Group, the German Participation Group, Harvard University, the Instituto de Astrofísica de Canarias, the Michigan State/Notre Dame/JINA Participation Group, Johns Hopkins University, Lawrence Berkeley National Laboratory, Max Planck Institute for Astrophysics, New Mexico State University, New York University, Ohio State University, Pennsylvania State University, University of Portsmouth, Princeton University, the Spanish Participation Group, University of Tokyo, University of Utah, Vanderbilt University, University of Virginia, University of Washington, and Yale University.

This work is based on archival data from the *Spitzer Space Telescope* available in the NASA/ IPAC Infrared Science Archive, which is operated by the Jet Propulsion Laboratory, California Institute of Technology, under contract with the National Aeronautics and Space Administration. Some of the data presented in this paper were obtained from the Mikulski Archive for Space Telescopes (MAST). STScI is operated by the Association of Universities for Research in Astronomy, Inc., under NASA contract NAS5-26555. Support for MAST for non-HST data is provided by the NASA Office of Space Science via grant NNX09AF08G and by other grants and contracts. This research has made use of different Python packages and of NASA’s Astrophysics Data (NED) System Bibliographic Services which is operated by the Jet Propulsion Laboratory, California Institute of Technology, under contract with the National Aeronautics and Space Administration.

We acknowledge constructive remarks by an anonymous referee.

REFERENCES

- Alam S., et al., 2015, *ApJS*, 219, 12
 Azzollini R., Trujillo I., Beckman J. E., 2008a, *ApJ*, 679, L69
 Azzollini R., Trujillo I., Beckman J. E., 2008b, *ApJ*, 684, 1026
 Bakos J., Trujillo I., Pohlen M., 2008, *ApJ*, 683, L103
 Bertin E., Arnouts S., 1996, *A&AS*, 117, 393
 Bertin E., Mellier Y., Radovich M., Missonnier G., Didelon P., Morin B., 2002, in Bohlender D. A., Durand D., Handley T. H., eds, *Astronomical Society of the Pacific Conference Series* Vol. 281, *Astronomical Data Analysis Software and Systems XI*. p. 228
 Bland-Hawthorn J., Gerhard O., 2016, *ARA&A*, 54, 529
 Buta R. J., et al., 2015, *ApJS*, 217, 32
 Comerón S., et al., 2012, *ApJ*, 759, 98
 Comerón S., Salo H., Knapen J. H., 2018, *A&A*, 610, A5
 Debattista V. P., Mayer L., Carollo C. M., Moore B., Wadsley J., Quinn T., 2006, *ApJ*, 645, 209
 Debattista V. P., Roškar R., Loebman S. R., 2017, *The Impact of Stellar Migration on Disk Outskirts*. *Astrophysics and Space Science Library*, Springer International Publishing, Cham, Switzerland, pp 77–114, doi:10.1007/978-3-319-56570-5_3
 Erwin P., 2015, *ApJ*, 799, 226
 Erwin P., Pohlen M., Beckman J. E., Gutiérrez L., Aladro R., 2008, in Knapen J. H., Mahoney T. J., Vazdekis A., eds, *Astronomical Society of the Pacific Conference Series* Vol. 390, *Pathways Through an Eclectic Universe*. p. 251 (arXiv:0706.3829)
 Fazio G. G., et al., 2004, *ApJS*, 154, 10
 Fliri J., Trujillo I., 2016, *MNRAS*, 456, 1359
 Florido E., Battaner E., Gros A., Prieto M., Mediavilla E., 1992, *Ap&SS*, 190, 293
 Grand R. J. J., Springel V., Gómez F. A., Marinacci F., Pakmor R., Campbell D. J. R., Jenkins A., 2016, *MNRAS*, 459, 199
 Han Z., Podsiadlowski P., Lynas-Gray A. E., 2007, *MNRAS*, 380, 1098
 Kennicutt Jr. R. C., 1989, *ApJ*, 344, 685
 Kroupa P., 2001, *MNRAS*, 322, 231
 Laurikainen E., Salo H., 2001, *MNRAS*, 324, 685
 Makarov D., Prugniel P., Terekhova N., Courtois H., Vauglin I., 2014, *A&A*, 570, A13
 Martín-Navarro I., et al., 2012, *MNRAS*, 427, 1102
 Martín-Navarro I., Trujillo I., Knapen J. H., Bakos J., Fliri J., 2014, *MNRAS*, 441, 2809
 Martin D. C., et al., 2005, *ApJ*, 619, L1
 Mathis J. S., 1990, *ARA&A*, 28, 37
 Minchev I., Quillen A. C., 2006, *MNRAS*, 368, 623
 Moré J. J., 1978, *Lecture Notes in Math.*, 630, 105
 Morrison H. L., Boroson T. A., Harding P., 1994, *AJ*, 108, 1191
 Morrissey P., et al., 2007, *ApJS*, 173, 682
 Muñoz-Mateos J. C., et al., 2015, *ApJS*, 219, 3
 Naeslund M., Joersaeter S., 1997, *A&A*, 325, 915
 Oliphant T. E., 2006, *All Faculty Publications*, 278
 Peters S. P. C., van der Kruit P. C., Knapen J. H., Trujillo I., Fliri J., Cisternas M., Kelvin L. S., 2017, *MNRAS*, 470, 427
 Pohlen M., Trujillo I., 2006, *A&A*, 454, 759
 Pohlen M., Dettmar R.-J., LÁijtticke R., Aronica G., 2002, *A&A*, 392, 807
 Querejeta M., et al., 2015, *ApJS*, 219, 5
 Radburn-Smith D. J., et al., 2014, *ApJ*, 780, 105
 Röck B., Vazdekis A., Peletier R. F., Knapen J. H., Falcón-Barroso J., 2015, *MNRAS*, 449, 2853
 Roškar R., Debattista V. P., Stinson G. S., Quinn T. R., Kaufmann T., Wadsley J., 2008a, *ApJ*, 675, L65
 Roškar R., Debattista V. P., Quinn T. R., Stinson G. S., Wadsley J., 2008b, *ApJ*, 684, L79
 Rupen M. P., 1991, *AJ*, 102, 48
 Salo H., et al., 2015, *ApJS*, 219, 4
 Sandin C., 2014, *A&A*, 567, A97
 Sandin C., 2015, *A&A*, 567, A106
 Schaye J., 2004, *ApJ*, 609, 667
 Sellwood J. A., 2014, *Reviews of Modern Physics*, 86, 1

- Sellwood J. A., Binney J. J., 2002, [MNRAS](#), 336, 785
 Sellwood J. A., Carlberg R. G., 1984, [ApJ](#), 282, 61
 Shang Z., et al., 1998, [ApJ](#), 504, L23
 Sheth K., et al., 2010, [PASP](#), 122, 1397
 Toomre A., 1963, [ApJ](#), 138, 385
 Trujillo I., Fliri J., 2016, [ApJ](#), 823, 123
 Trujillo I., Pohlen M., 2005, [ApJ](#), 630, L17
 Trujillo I., Aguerrí J. A. L., Cepa J., Gutiérrez C. M., 2001a, [MNRAS](#), 321, 269
 Trujillo I., Aguerrí J. A. L., Cepa J., Gutiérrez C. M., 2001b, [MNRAS](#), 328, 977
 Trujillo I., et al., 2004, [ApJ](#), 604, 521
 Trujillo I., et al., 2006, [ApJ](#), 650, 18
 Vazdekis A., Koleva M., Ricciardelli E., Röck B., Falcón-Barroso J., 2016, [MNRAS](#), 463, 3409
 Wu H., et al., 2002, [AJ](#), 123, 1364
 Zaritsky D., et al., 2013, [ApJ](#), 772, 135
 Zibetti S., White S. D. M., Brinkmann J., 2004, [MNRAS](#), 347, 556
 de Jong R. S., 2008, [MNRAS](#), 388, 1521
 de Jong R. S., et al., 2007, [ApJ](#), 667, L49
 van der Kruit P. C., 1979, [A&AS](#), 38, 15
 van der Kruit P. C., 1987, [A&A](#), 173, 59
 van der Kruit P. C., Freeman K. C., 2011, [ARA&A](#), 49, 301
 van der Kruit P. C., Searle L., 1981a, [A&A](#), 95, 105
 van der Kruit P. C., Searle L., 1981b, [A&A](#), 95, 116

APPENDIX A: SURFACE BRIGHTNESS PROFILES

In the following figures, we plot the radial surface brightness profiles for each galaxy, in each wavelength range and at different heights above/below the galaxy mid-plane. We plot all the surface brightness profiles of a galaxy, in a given band, together, so as to highlight the variations of the truncation position along the vertical axis. Then, we show the same kind of plot but for a PSF-deconvolved model of each galaxy in the optical SDSS *gri* combined band.

In all panels of each figure, the black line shows the mid-plane surface brightness profile. The vertical dark grey region always represents the mean position of the truncation for all the heights in the wavelength range, plus/minus the standard deviation of that distribution of truncation positions. From top to bottom and from left to right, the panels show in red the surface brightness profile at a given altitude above the galaxy mid-plane (indicated in the legend) and, in light grey, the surface brightness profiles plotted in the previous panels.

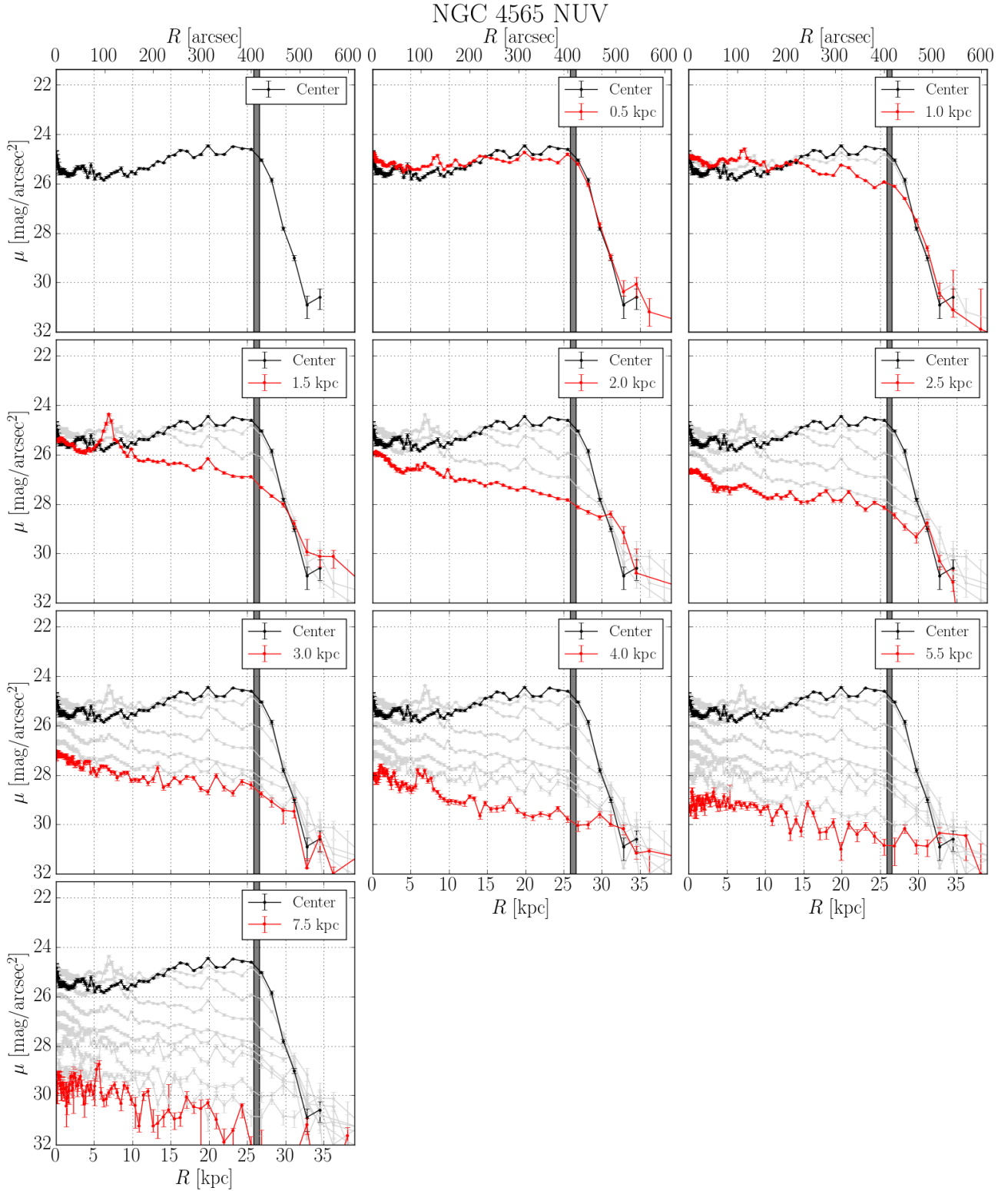


Figure A1. Vertical development of the radial surface brightness profiles in the NUV band for NGC 4565. The mean of the truncation position distribution is equal to 26.2 kpc and the standard deviation is 0.4 kpc.

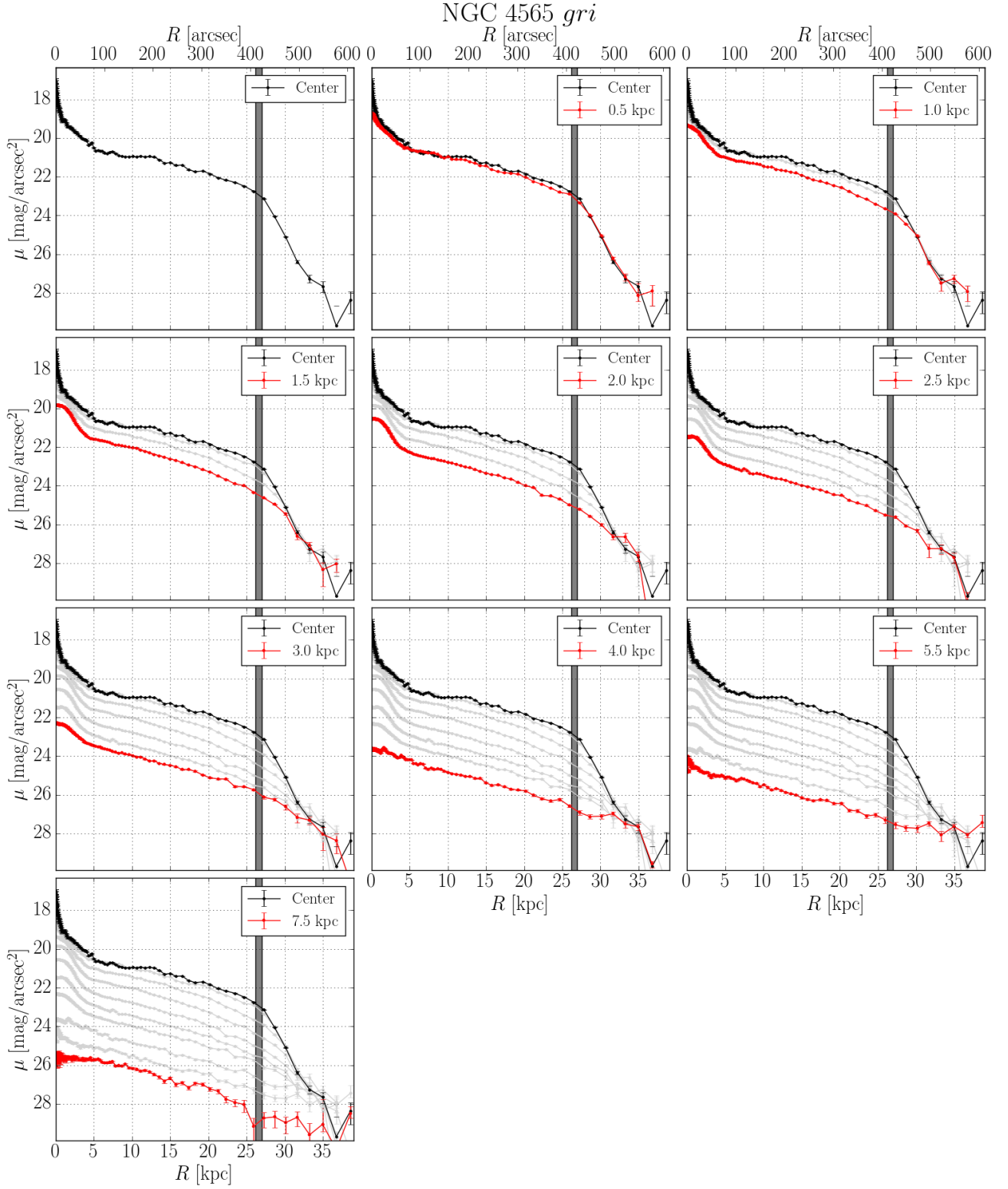


Figure A2. As in Fig. A1, now for the *gri* combined band. The mean of the truncation position distribution is 26.6 kpc and the standard deviation is 0.4 kpc.

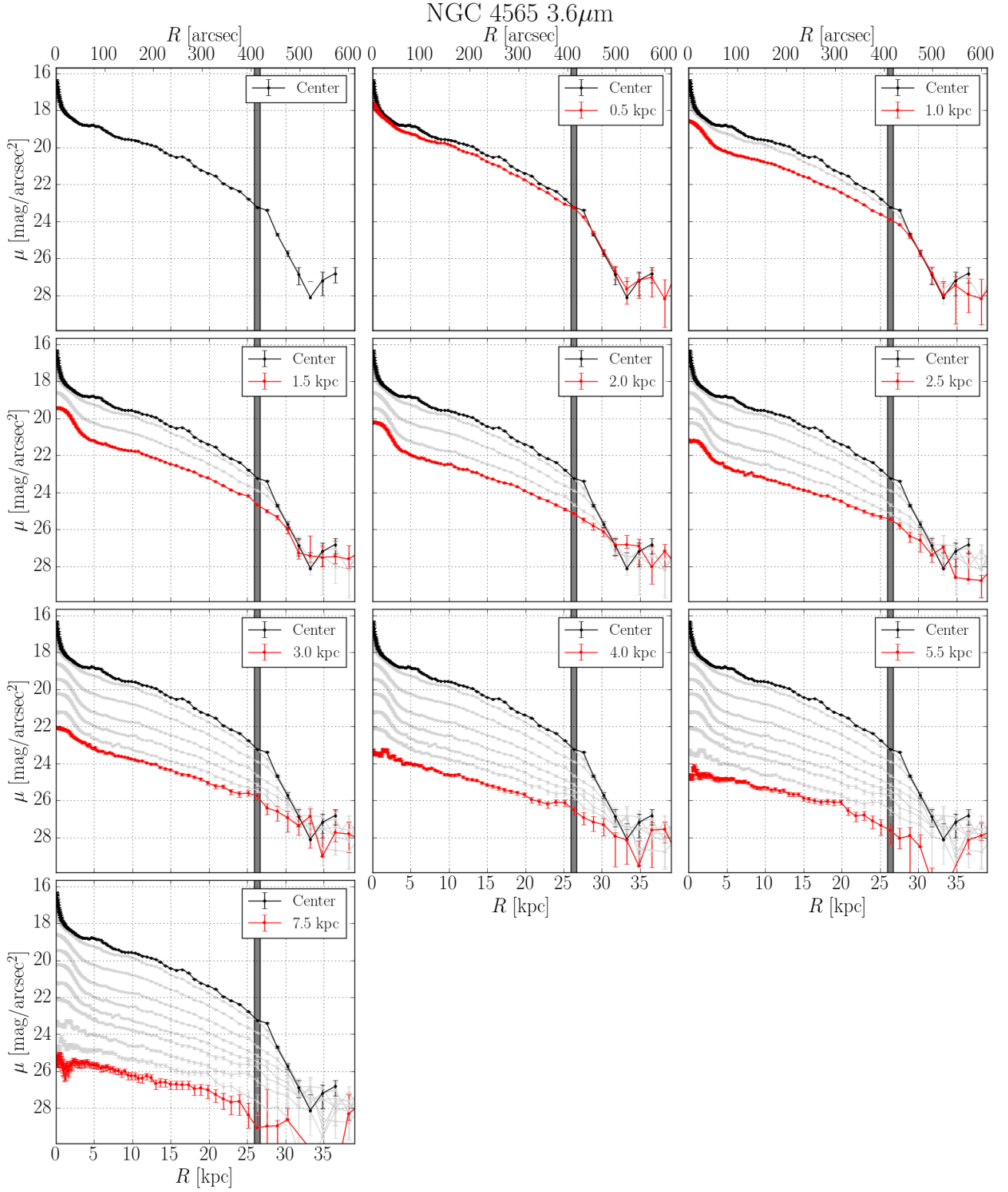


Figure A3. As in Fig. A1, now in $3.6\mu\text{m}$. The mean of the truncation position distribution is 26.3 kpc and the standard deviation is 0.4 kpc.

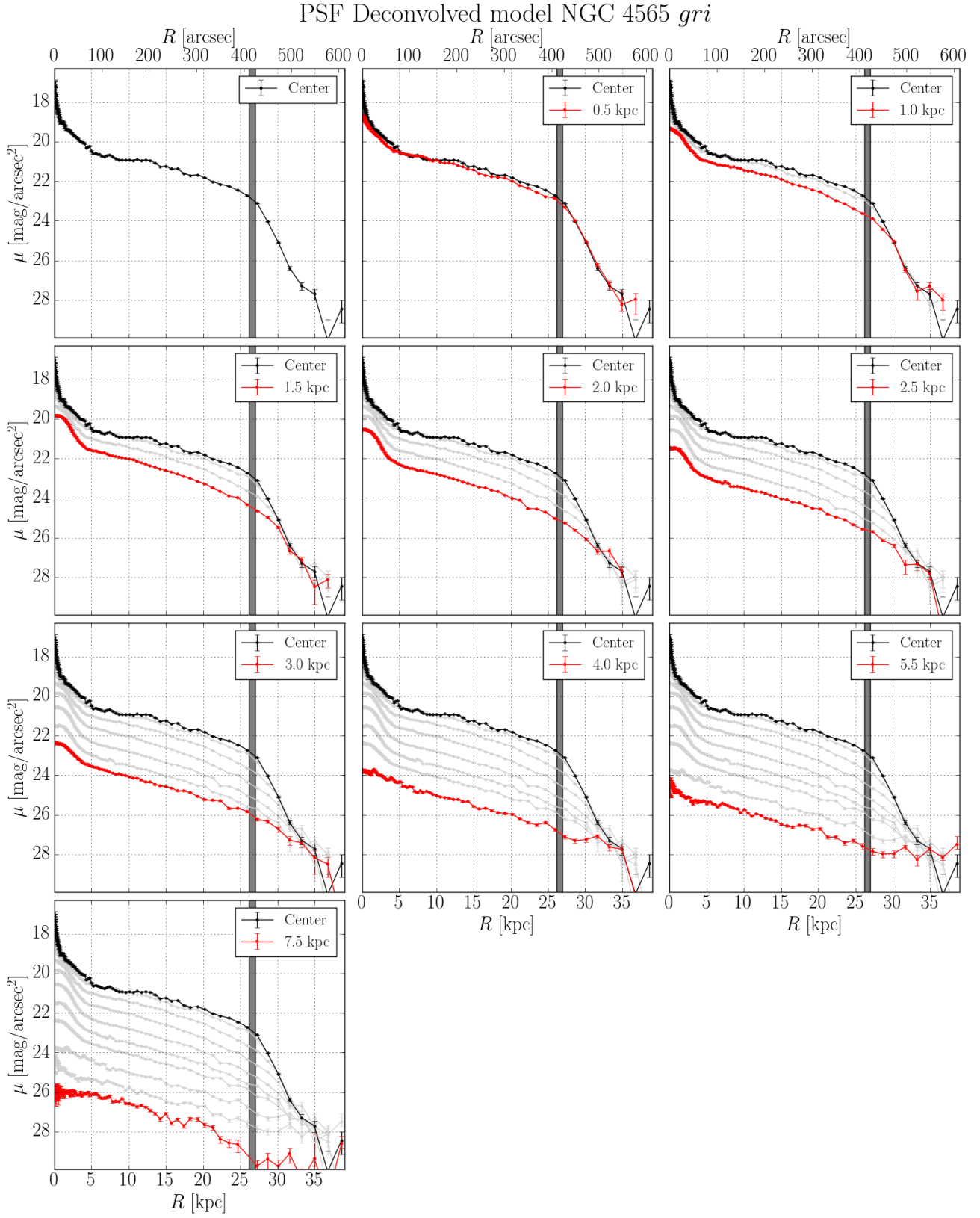


Figure A4. As in Fig. A1, but for the NGC 4565 PSF-deconvolved model in *gri*. The mean of the truncation position distribution is the same as in A2.

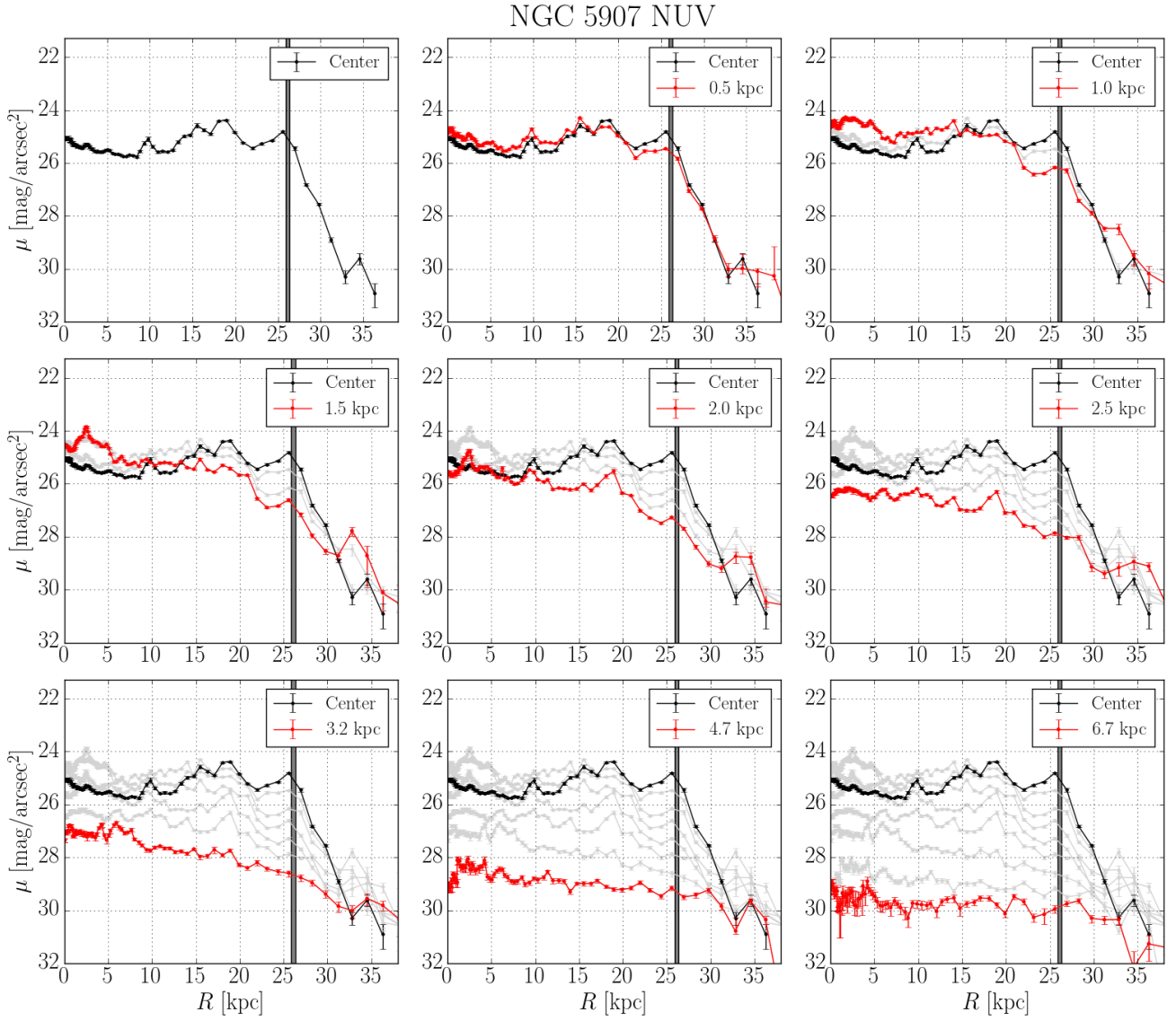


Figure A5. As in Fig. A1, now for NGC 5907 in NUV band. The mean of the truncation position distribution is 26.1 kpc and the standard deviation is equal to 0.2 kpc.

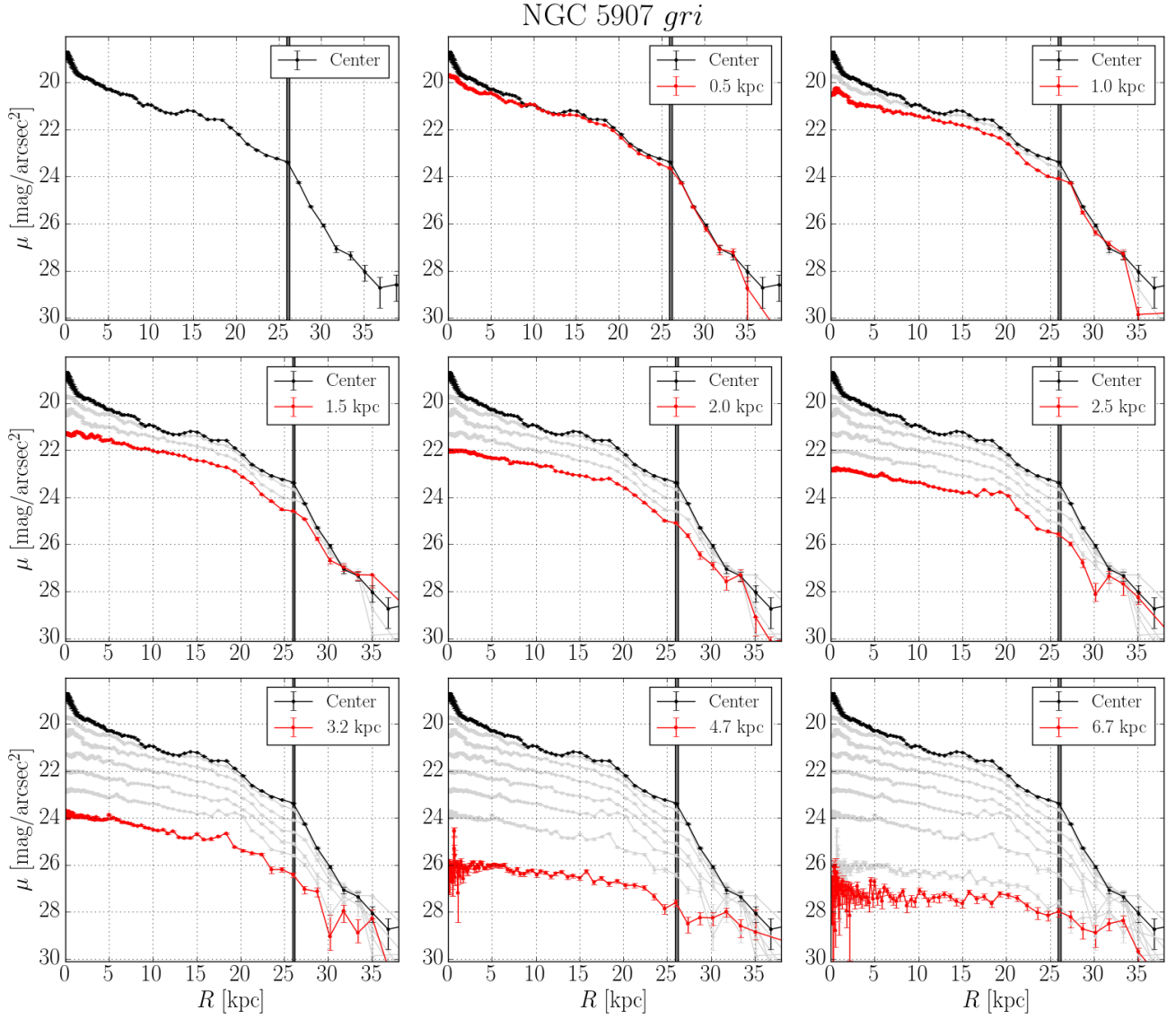


Figure A6. As in Fig. A1, now for NGC 5907 in the *gri* combined band. The mean of the truncation position distribution is equal to 26.1 kpc and the standard deviation is 0.2 kpc.

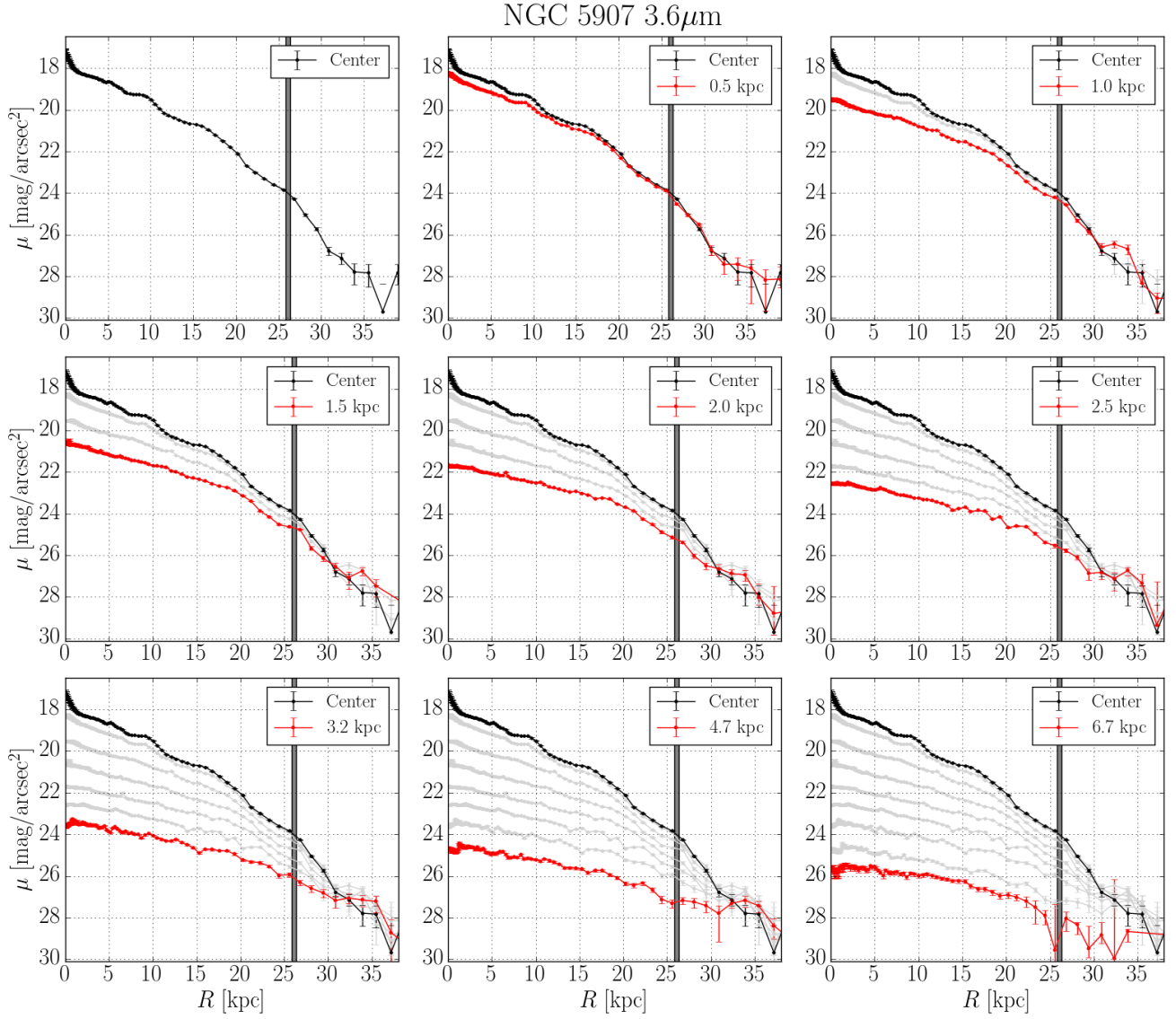


Figure A7. As in Fig. A1, but for NGC 5907 in $3.6\mu\text{m}$. The mean of the truncation position distribution is 26.1 kpc and the standard deviation is 0.3 kpc.

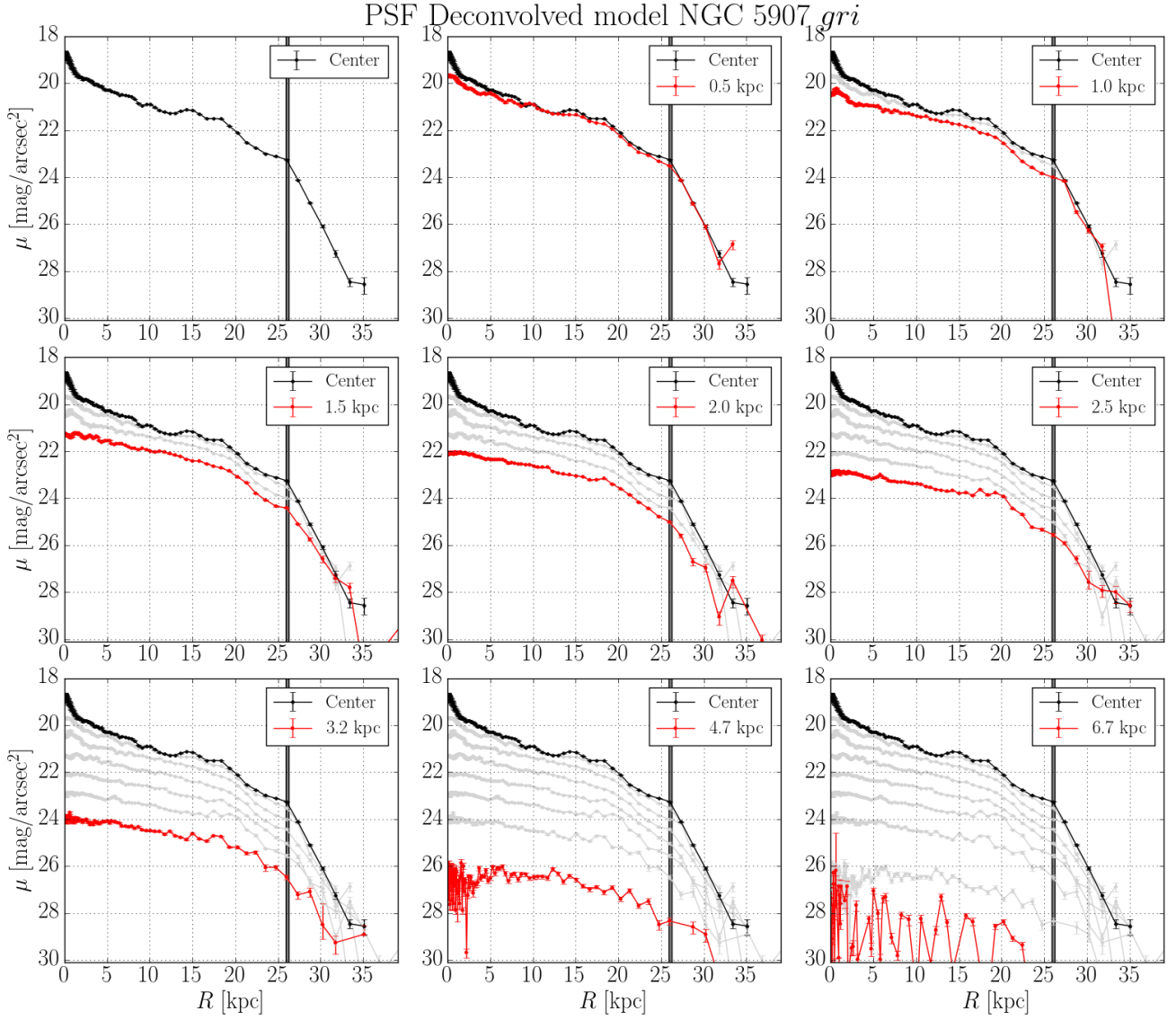


Figure A8. As in Fig. A1, but for the PSF-deconvolved model of NGC 5907 in *gri*. The mean of the truncation position distribution is the same as in A6.

**APPENDIX B: EXAMPLE OF SURFACE
BRIGHTNESS PROFILES ABOVE AND BELOW
THE GALAXIES MID-PLANE SEPARATELY**

from a perfect edge-on inclination of the galaxies. This is more clearly visible in the case of NGC 5907.

In the next figure, we plot radial surface brightness profiles for each galaxy, in the *gri* band, at three different heights: along the galaxy mid-plane, at 1.5 kpc and at 3 kpc. In each case, we show the surface brightness profiles obtained above the mid-plane of the galaxies (northeastwards, NE), below it (southwesterly, SW) and the mean of both, that is the actual surface brightness profile we show in all the plots of this paper. Here we see that the truncation position is the same in both sides of the galaxies, so using the mean profile in our analysis is a reasonable approach. Note that the main difference is a slight brightness offset between the above and below mid-plane profiles caused by departures

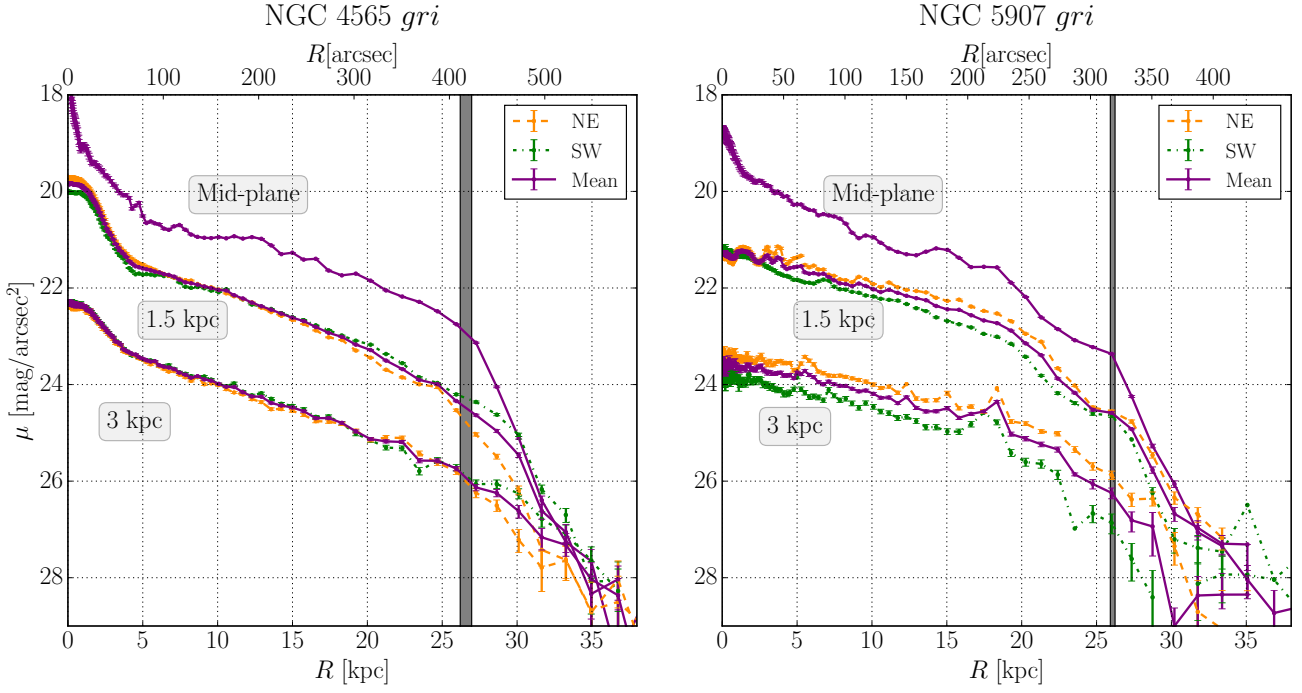


Figure B1. Radial surface brightness profiles in the *gri* combined band for both galaxies along the mid-plane, at 1.5 kpc and 3 kpc above/below the mid-plane. In the two panels of the figure, the purple solid curves show the mean surface brightness profile at each height (in the case of the mid-plane profile is the only possibility). The orange dashed curves represent the profiles above the mid-plane of the galaxies (north-eastwards, NE) and the green dotted lines are the profiles below the mid-plane (south-westerly, SW). The height of each set of surface brightness profiles is indicated with the light grey boxes. The vertical dark grey region always represents the mean position of the truncation for all the heights in the wavelength range, plus/minus the standard deviation of that distribution of truncation positions.

APPENDIX C: EXAMPLE OF SURFACE BRIGHTNESS PROFILES IN REGIONS WITH AND WITHOUT WARP

In Figs. C1 and C2, we show images in the SDSS *gri* combined band of NGC 4565 and NGC 5907, respectively. We indicate the regions of each galaxy in which the warps are located by splitting the images into four quadrants (Q1, Q2, Q3, and Q4). We then show surface brightness profiles taken in those four quadrants in Fig. C3.

In Fig. C3, we plot the radial surface brightness profiles in the warped and non-warped regions for each galaxy, in all wavelength ranges (NUV, *gri*, and $3.6\mu\text{m}$), and at two different heights above/below the galaxy mid-plane: 0.5 kpc and 2 kpc. The surface brightness profiles are 0.5 kpc width.

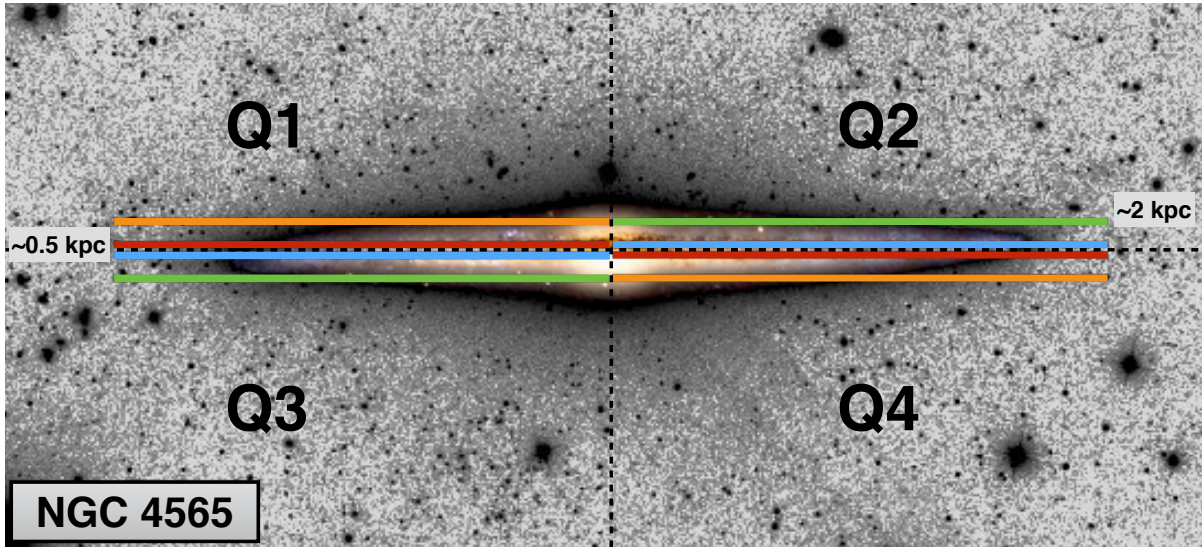


Figure C1. Image of NGC 4565 in SDSS *gri* combined light (roughly equivalent to a deep *r*-band image). For illustrative purposes, a colour image obtained with the same telescope has been inserted atop the saturated disc region of the galaxy. Panels show in greyscale the observed data. The image is split into four quadrants (Q1, Q2, Q3, and Q4). In this galaxy, Q2 and Q3 are the regions with a warp, while Q1 and Q4 are the warp-free areas. The horizontal thick coloured lines indicate the regions where the surface brightness profiles in Fig. C3 were taken. The profiles closer to the galaxy's mid-plane are at 0.5 kpc height, while those above are located at 2 kpc.

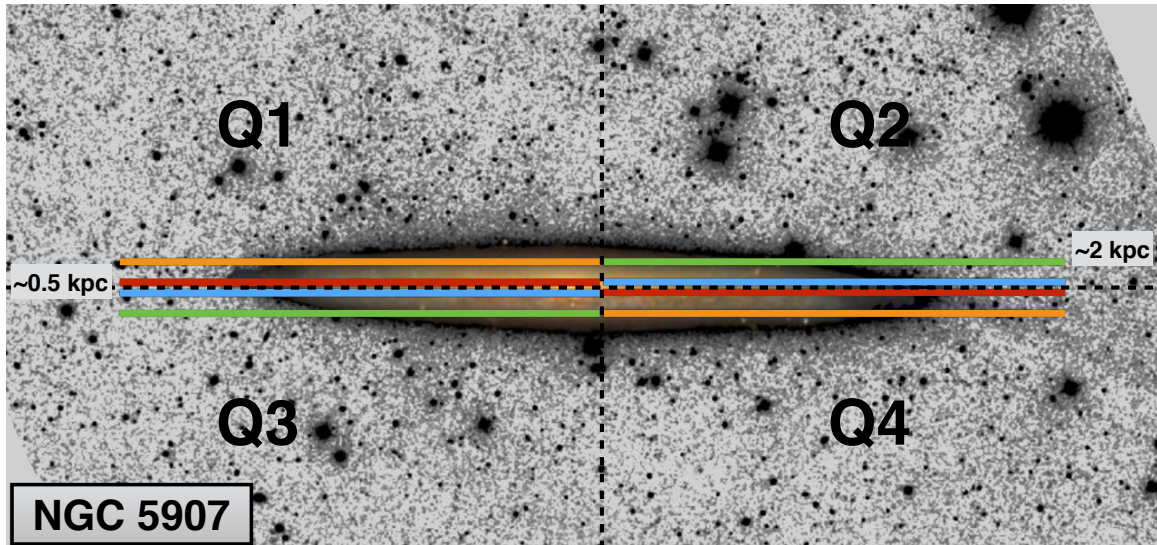


Figure C2. As in Fig. C1, but now for NGC 4565. In this galaxy, Q1 and Q4 are the regions with a warp, while Q2 and Q3 are the warp-free areas.

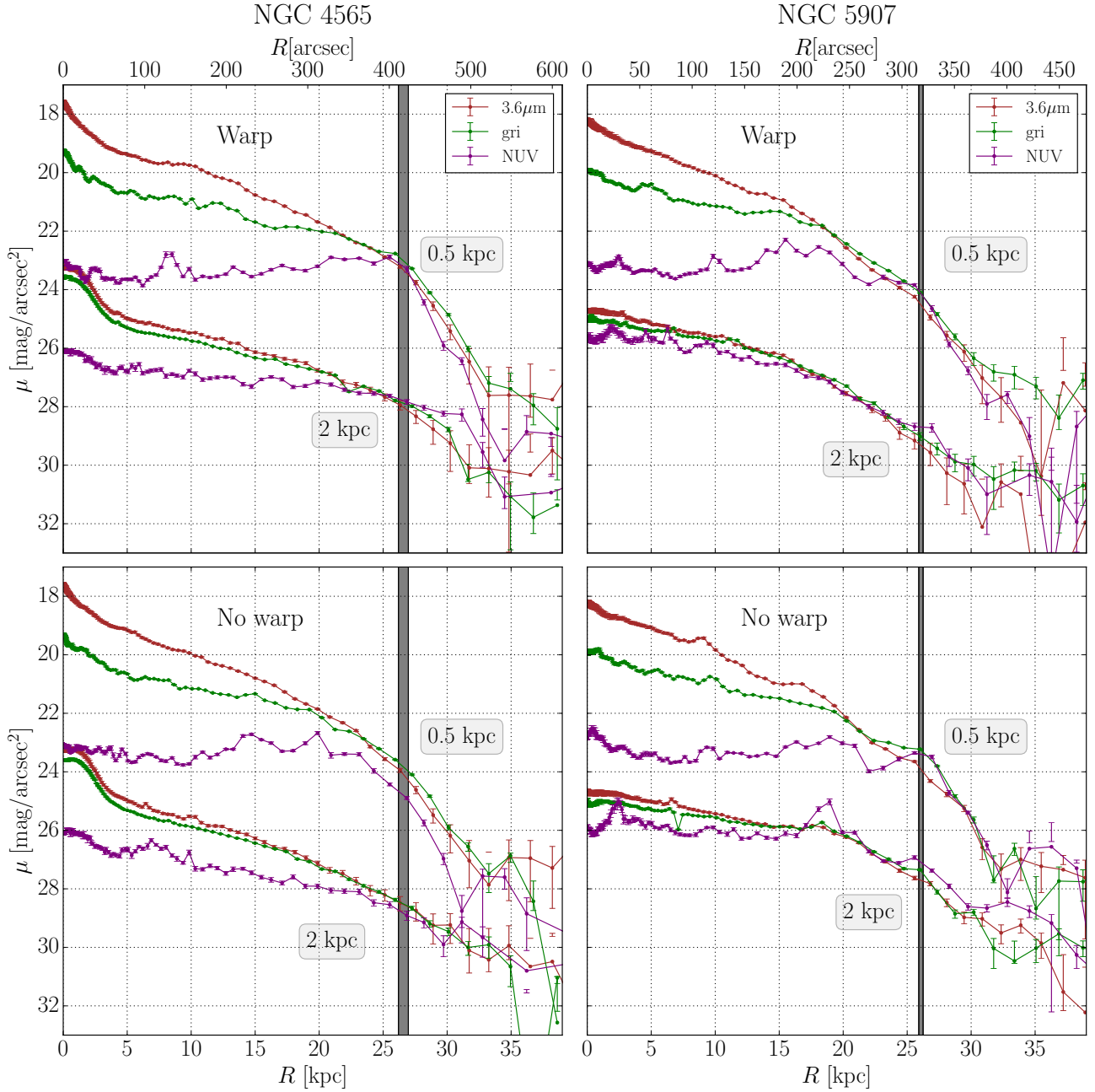


Figure C3. Radial surface brightness profiles obtained from the observed data of each galaxy, NGC 4565 (left column) and NGC 5907 (right column), at two different heights above/below the galaxy mid-plane (0.5 kpc and 2 kpc), in the NUV, *gri*, and $3.6\mu\text{m}$ bands, for the warped (top row) and non-warped (bottom row) regions separately. For NGC 4565, the warped region corresponds to quadrants Q2 and Q3 in Fig. C1. Thus, the surface brightness profiles at 0.5 kpc correspond to the blue thick lines, and the ones at 2 kpc, to the green lines shown in Fig. C1. Q1 and Q4 are the non-warped regions in NGC 4565, and the red and orange lines in Fig. C1 indicate the locations we used to obtain the 0.5 kpc and 2 kpc surface brightness profiles. We proceed identically for NGC 5907, but considering that Q1 and Q4 are the quadrants with a warp in Fig. C2, so in Q2 and Q3 there is no warp. The surface brightness profiles are obtained using regions with 0.5 kpc width. The vertical dark grey region represents the mean position of the truncation for all the heights in the SDSS *gri* combined band for each galaxy, plus/minus the standard deviation of that distribution of truncation positions.

This paper has been typeset from a T_EX/L^AT_EX file prepared by the author.